The Thesis committee for Timothy Daniel Klatt
certifies that this is the approved version of the following thesis:

Extreme Energy Absorption: The Design, Modeling, and Testing of Negative Stiffness Metamaterial Inclusions

APPROVED BY

SUPERVISING COMMITTEE:

Carolyn C. Seepersad, Supervisor

Michael R. Haberman, Co-supervisor

Extreme Energy Absorption: The Design, Modeling, and Testing of Negative Stiffness Metamaterial Inclusions

by

Timothy Daniel Klatt, B.A.; B.S.M.E.

THESIS

Presented to the Faculty of the Graduate School of

The University of Texas at Austin

in Partial Fulfillment

of the Requirements

for the Degree of

MASTER OF SCIENCE IN ENGINEERING

The University of Texas at Austin

August 2013

To Jesse, Ogden & Amity,

my loving family that inspires me endlessly.

Extreme Energy Absorption: The Design, Modeling, and Testing of Negative Stiffness Metamaterial Inclusions

Timothy Daniel Klatt, M.S.E.
The University of Texas at Austin, 2013

Supervisors: Carolyn C. Seepersad
Michael R. Haberman

A persistent challenge in the design of composite materials is the ability to fabricate materials that simultaneously display high stiffness and high loss factors for the creation of structural elements capable of passively suppressing vibro-acoustic energy. Relevant recent research has shown that it is possible to produce composite materials whose macroscopic mechanical stiffness and loss properties surpass those of conventional composites through the addition of trace amounts of materials displaying negative stiffness (NS) induced by phase transformation [R. S. Lakes, et al., Nature, **410**, pp. 565-567, (2001)]. The present work investigates the ability to elicit NS behavior without employing physical phenomena such as inherent nonlinear material behavior (e.g., phase change or plastic deformation) or dynamic effects, but rather the controlled buckling of small-scale structural elements, metamaterials, embedded in a continuous viscoelastic matrix. To illustrate the effect of these buckled elements, a nonlinear hierarchical multiscale material model is derived which estimates the macroscopic stiffness and loss of a composite material containing pre-strained microscale structured inclusions. The nonlinear multiscale model is then utilized in a set-based hierarchical design approach to explore the design space over a wide range of inclusion

geometries. Finally, prototype NS inclusions are fabricated using an additive manufacturing technique and tested to determine quasi-static inclusion stiffness which is compared with analytical predictions.

Table of Contents

Chapter 1

Introduction

1.1 Motivation for High Stiffness, High Loss Materials

Unwanted mechanical energy is pervasive. Components of mechanical systems vibrate, oscillate, and shake, generating energy that the system must accommodate. These loads tend to lead to either over-engineering or decreased lifespan of the system. Conventional methods of dealing with mechanical energy include "brute force" methods like increasing the stiffness or mass of the structure, coupling the load to less vibration-susceptible components, or more sophisticated methods like creating structural elements from engineering composites that possess increased damping.

Consider the stiffness-loss map in Fig. 1.1 from Brodt and Lakes [1], which depicts the stiffness (Young's modulus, represented in the plot as E, but as Y elsewhere in this thesis) and loss (represented by $\tan\delta$) of common materials. Generally speaking, stiff materials are not very absorptive, and vice versa. Furthermore, composites and some polymers can exhibit both moderate stiffness and loss, but there appears to be a limit to these characteristics, as depicted by the dashed line in the upper-right quadrant of the Fig. 1.1. The goal of recent research has been to populate the so-called "white space" of the upper-right quadrant of the plot with materials possessing both high stiffness and high loss.

Recent developments in the field of traditional composites has shown that composites containing a small volume fraction of negative stiffness (NS) inclusions can theoretically lead to overall extreme stiffness and damping [2]. The basis for NS

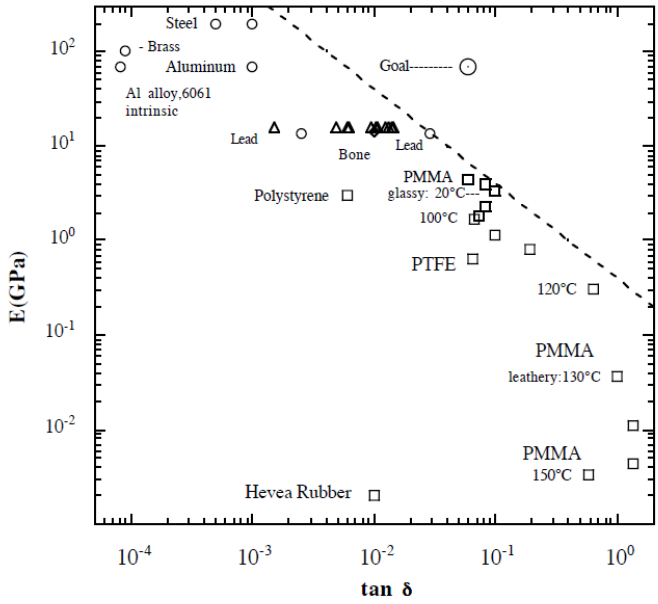

Figure 1.1: Stiffness-loss map for some common materials, reprinted from Brodt and Lakes [1].

inclusions leading to increased damping lies in the unique stress-strain relationship of NS systems which yields dramatically greater strain localized about the NS domain within the composite material [2]. This theory has been validated by recent experimentation of materials with microscale inclusions possessing thermally-activated energy wells resulting from phase transformations [2]. Work by Kashdan [3, 4] and Fulcher [5] have experimentally demonstrated the increased vibration and shock isolation and absorption capabilities of systems containing macroscale NS elements, further motivating the study of NS components. Taking inspiration from these macroscale elements, acoustic metamaterials, defined as materials whose properties are derived from sub-wavelength structure and not necessarily constituent materials properties, represent one path to attain NS with sub-wavelength structures. While some recent work has demonstrated notional topology optimization schemes for negative compressibility [6, 7], no manufacturable designs of small-scale inclusions demonstrating NS exist in the literature. Thus, the focus of this thesis is to explore and create paths

for producing these small-scale energy absorbing inclusions.

1.2 Objectives

The objectives of this research are to model, design, build and test NS metamaterial inclusions that can be employed to create composite materials demonstrating increased vibro-acoustic energy absorbing capacity on the macroscale. To achieve these objectives, this thesis has followed the approach outlined here:

- **Multiscale Material Model Development**. The design problem investigated in this work is inherently multiscale and requires models to be developed and benchmarked at each length scale in order to accurately model the effects of small-scale NS metamaterial inclusions on macroscale composite material properties. Nonlinear finite element strain energy methods are employed to obtain nonlinear stiffness properties of small-scale embeddable structures based on structural buckling phenomena. Classical effective medium theory models are employed in determining the macroscale response of a composite material with NS inclusions.

- **Set-Based Hierarchical Design Space Exploration**. In order to explore the design space of this new approach of engineering energy absorbing materials, a multiscale material model is developed and implemented into an iterative design loop to map the design and performance space of a composite material containing NS inclusions.

- **Prototype Inclusion Design, Fabrication, and Test**. An alternative approach to producing NS elements is investigated and proof of concept NS elements are built using selective laser sintering. These prototype NS inclusions

are tested to determine the quasi-static inclusion stiffness and compare their performance with analytical predictions.

1.3 Overview of Research and Thesis

This thesis is organized in three main sections: (1) modeling the elastic response of NS inclusions and multiscale composite materials containing such inclusions, (2) utilizing an iterative design loop to map the performance and design spaces at each particular scale, and (3) designing and testing prototype NS inclusions. The following paragraphs describe the work presented in this thesis.

The first step in the **multiscale modeling** of an energy absorbing composite material containing NS inclusions is to create models that provide accurate estimates of the elastic response of the system. The modeling approach presented in this work is inherently multiscale. That is, the microscale features of the inclusion lead to a mesocale stiffness of a representative volume element, which in turn leads to a macroscale stiffness and loss for vibro-acoustic loading of a composite material consisting of a matrix and inclusions of certain volume and orientation. Thus, models are created to study the characteristics at each of the scales and to link material behavior and composition at one scale to the properties observed at the next.

This multiscale material model is the subject of Chapter 3. A candidate NS metamaterial inclusion is presented in Sec. 3.2 along with a description of the multiscale modeling approach in Sec. 3.3. Section 3.4 presents the micro $\rightarrow$ meso scale transition model development and results of an energy-based approach to determining the nonlinear mesoscale inclusion stiffness. The meso $\rightarrow$ macro scale transition model used in this work employs effective medum theory models to demonstrate the effect of microscale NS inclusions on the energy absorption of a macroscale composite material,

and is presented in Sec. 3.5.

Chapter 4 presents the **hierarchical design** of composite materials with NS inclusions. The micro $\rightarrow$ meso scale transition model presented in Sec. 3.4 is employed to obtain the nonlinear mesoscale stiffness of a parameterized geometry over a wide range of parameter values. Section 4.3 demonstrates how metamodeling techniques, which are essentially arbitrary functions that are fitted to data points in order to provide estimates of system response, can be applied to the design problem. A metamodel is used to produce maps of the design and performance space of the parameterized inclusion geometry at the mesoscale. These results are then propagated forward to the next scale, and design and performance maps of the meso $\rightarrow$ macro scale transition model are presented in Sec. 4.4. A multilayer beam system is presented in Sec. 4.5 and used to demonstrate the effect of an optimized beam coating consisting of NS inclusions on the beam ringdown and shock response.

Finally, Chapter 5 documents the **design, build, and test** of prototype NS inclusions. Section 5.1 introduces the idea of obtaining NS via a curved beam geometry, as well as the design and fabrication of such an element. Here, an additive manufacturing technique is used to produce prototype NS inclusions. These elements are tested to obtain the quasi-static force-displacement relationships, and test results are compared with the analytical predictions in Sec. 5.2. These results validate the approach of obtaining NS via a curved beam geometry.

Chapter 2

Review of Literature and Principles

2.1 Introduction

There are numerous applications requiring structural or coating materials with an elevated capacity to absorb mechanical energy. Specific examples include sonar transducer backing and baffle materials, rotor blades, automobile chassis, motor mounts, and aircraft fuselages. In many cases, an ideal absorbing material would be characterized by a simultaneously large loss factor, η, (often found in soft polymers) and high stiffness, $\mathbf{C}$, (typical of metals and ceramics). Indeed, some existing absorptive materials are created by embedding stiff inclusions in a soft viscoelastic matrix in an effort to achieve this ideal combination of material properties [8]. Unfortunately, physical bounds limit the achievable effective material properties of the composite to fall somewhere in between the material properties of each constituent [9–11]. As such, traditional design of absorptive composite materials possesses an inherent trade-off between achieving materials displaying high loss with low stiffness or high stiffness with low loss.

Another common difficulty in the design of absorptive materials and structures is the desire to provide effective energy absorption across a broad range of frequencies. Thus, a key technical challenge is to develop stiff, absorptive materials that exhibit high mechanical loss over a broad band of frequencies. Recent research in the field of composite materials has shown that it is theoretically possible to produce materials whose macroscopic mechanical stiffness and loss properties surpass those

of conventional composites when small portions (1–2% by volume) of NS domains are embedded into a continuous host material [2, 12, 13]. It is therefore of interest to investigate means to produce negative stiffness (NS) inclusions that are designed for specific applications of scientific interest. Achieving NS behavior by design, however, is a nontrivial task.

The concept of NS is currently of high interest primarily due to the works of Lakes and co-workers [2, 12, 13] and the field of acoustic metamaterials [14–16] where the dynamic behavior of 'materials' with hidden degrees of freedom display negative effective density and stiffness. However, it is worth noting that the concept of NS has been of interest for nearly two centuries. Notably, the contractile aether introduced by Cauchy's third theory on the reflection of light [17] and described in detail by William Thomson (Lord Kelvin) [18] required an elastic medium with negative compressibility to eliminate the existence of longitudinal light waves [19].

Examples of NS mechanisms include mechanical systems with bistable configurations [6] and materials with negative moduli [2, 12]. NS elements contribute to damping behavior because they tend to assist rather than resist deformation as a result of internally stored energy [2, 12]. Experiments have shown cells containing a buckled silicone rubber tube achieved damping that was significantly larger than the unbuckled system under sinusoidal forcing. Furthermore, studies of multiwalled carbon nano-tubes have shown that buckled tube components achieve higher damping than unbuckled tubes in the nano-scale [20]. Wang and Lakes [21] also showed that higher damping can be achieved through the use of inclusions possessing negative bulk modulus. Though the concept of using embedded NS domains in a material system was indeed an excellent and non-intuitive observation, NS mechanisms had been previously explored for vibration reduction systems. For example, Minus K

technologies has implemented these elements into isolation tables to reduce environmental sub-Hertz vibrations [22]. These systems require the use of electromechanical adjustment systems to ensure that the isolation will be sufficient for any weighted system. A second method for creating vibration isolation systems using NS systems employs the principle that two springs in parallel with the same stiffness magnitude, but opposite signs will approach infinite stiffness [23]. This application, like many, orients the NS systems in the axial direction for vibration reduction. The present work focuses on the analysis of small-scale structures that employ concepts similar to those introduced in the field of vibration isolation which can be scaled down to be embedded in a lossy matrix to produce a heterogeneous composite material with NS metamaterial inclusions.

Additionally, it is interesting to note that NS structures have been evaluated for other applications, including the ability to increase both the stiffness and overall damping capacity of a material. For example, Prasad and Diaz [6] used topology optimization to create microscale NS arrays with the possibility that they could become NS cellular materials. Buckled beam elements have also been used in microelectromechanical systems (MEMS) devices as switches for micromachined mirror logic systems [24, 25].

2.2 Negative Stiffness

A general definition of stiffness is the ability of a system (e.g., a structure or continuous material) to offer resistance to deformation when subjected to externally applied forces. Whereas positive stiffness systems offer increasing resistance to deformation, an NS system offers decreasing resistance and can even assist the applied force in deforming the system [26, 27]. NS systems will undergo significantly larger

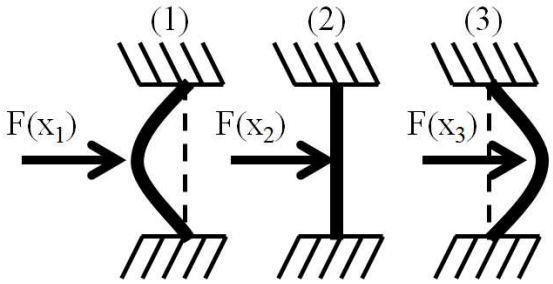

Figure 2.1: Schematic of the behavior of a beam of original length L_0 and buckled length $L_0 - \delta L$.

deformation than would a positive, or even a zero, stiffness system under the same loading conditions.

2.2.1 A Buckled Beam

As an illustrative example, consider the case of a simple system known to exhibit NS: a buckled beam. Figure 2.1 shows the scenario where a compressive axial displacement of sufficient magnitude to buckle the beam is imposed at its ends while no other constraints are applied. Under these conditions, the beam bows into one of two stable positions, configurations (1) or (3).

Figure 2.2a shows the normalized force versus displacement of the beam center point when transversely loaded in both displacement and force control. The normalized force is given as $2F/P_{cr}$, where F is the transversely applied load and P_{cr} is the axial load that induces buckling as predicted by Euler-Bernoulli beam theory. The normalized displacement is $\Delta x/2L_0$, where Δx is the displacement from the $x = 0$ position and L_0 is the free beam length. There are several points illustrated in these curves that are worth highlighting. First of all, note that positions (1), (2), and (3) all represent configurations where zero force is required to maintain that particular configuration. These are equilibrium positions that can be qualified through inspection

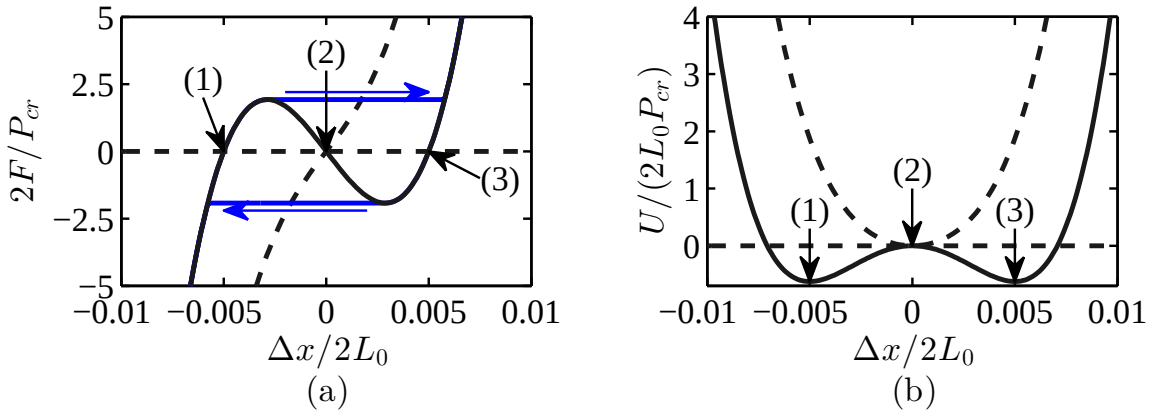

Figure 2.2: Normalized (a) force and (b) internal (strain) energy versus normalized displacement for a buckled (solid lines) and unbuckled (dashed lines), adapted from Saif [25]. Results indicate response for both displacement- (black line) and force-controlled loading (blue line), with arrows indicating direction of force-controlled loading.

of the internal energy, $U(x)$, versus displacement curve shown in Fig. 2.2b. Namely, these positions correspond to points of zero slope on the strain energy curve, i.e., $\partial U(x)/\partial x = 0$. This is not surprising since mechanics relates internal energy $U(x)$, force $F(x)$, and stiffness $k(x)$ through the relations [28]:

$$F(x) = \frac{\partial U(x)}{\partial x};\ k(x) = \frac{\partial F(x)}{\partial x} = \frac{\partial^2 U(x)}{\partial x^2}. \tag{2.1}$$

Since configurations (1) and (3) are equivalent from an energy standpoint, a beam in this loading scenario is in a bistable state. Assuming the beam starts from configuration (1), if one were then to subsequently impose a rightward transverse displacement at the midpoint of the beam from point (1) shown in Fig. 2.2a, it will initially resist deformation by requiring increasing force for increasing displacement increments until some critical displacement is reached, approximately half-way between points (1) and (2). Beyond this point, the beam will require decreasing force levels for increasing imposed lateral displacement. A decrease in force level requirement to impose an increase in displacement is a direct manifestation of NS behavior. This

trend continues until the beam is displaced to approximately half-way between points (2) and (3) in Fig. 2.2a, at which point it again displays positive stiffness and the second stable position is reached at position (3) which is a mirror displacement from the unbuckled beam axis at the starting point, position (1). Note that the behavior described above represents the case of displacement control loading. Displacement control is an ideal scenario where the external loading is assumed to provide any force level necessary to produce an increased displacement increment.

The converse idealized loading condition is known as force control. In force control, the external system is assumed to be capable of generating arbitrary displacements in order to permit increasing force increments. Under transversely imposed force control, one observes different behavior than just described under the displacement control scenario which directly displayed NS. Specifically, again starting from position (1), the increasing applied transverse force leads to incrementally increasing displacements towards the right. However, once a critical force level is achieved (corresponding to the point of zero stiffness in displacement control loading), the beam will then snap from a position to the left of the axis of the undeformed beam to the right where the beam once again requires a positive force increment for increased displacement. This behavior, often called snap-through, is indicative of bistable systems subjected to force controlled loading and is an indication that the system can be used to produce NS. Under unconstrained force controlled loading, snap-through is a transient event that leads to large and unrecoverable system deformations absent further loading in the opposite direction. Thus, the previous discussion indicates that axial loading of a beam can lead to buckling and bistability, and that subsequent transverse loading at the beam center-point can be employed for switching between the two stable configurations under force control or NS under displacement control.

Although positions (1), (2), and (3) are considered equilibria, physical intuition suggests that if one were to place the beam in position (2), it would not remain there when constraining forces are removed. This is because that the position is not unconditionally stable; rather, it is an unstable equilibrium condition. For unconditional stability, the change in the internal energy resulting from perturbations about the stable configuration must be positive. Mathematically this means that the curvature of the internal energy curve (i.e., the stiffness) must be positive, $\partial^2 U(x)/\partial x^2 > 0$. This requirement implies that any stable position is one where the strain energy is at a local minimum, also known as an energy well. Using these criteria, stability occurs at positions (1) and (3) where the slope of the internal energy curve is zero, $F(x) = \partial U(x)/\partial x = 0$, and where its curvature is positive: $\partial^2 U(x)/\partial x^2 = k(x) > 0$. The other position of interest, configuration (2), is an unstable equilibrium state, characterized as a point of zero force where the curvature of the internal energy curve is negative, i.e., a local maximum in the strain energy of the beam. Any unconstrained beam in this configuration will immediately be driven to one of the two unconditionally stable positions by any minor perturbation.

2.2.2 Constrained Negative Stiffness

Though a buckled beam in configuration (2) is unstable, there is a scenario whereby a buckled element can be exploited to produce NS in a useful manner. Consider a modification to the system where the beam is now constrained at its center point by a spring. In this case, as the axial deformation is imposed to induce buckling, the beam can remain in position (2) of Fig. 2.1 but is able to move when perturbed by an outside force. When an external force is applied, the constraining element will return the beam to position (2) when the outside force is removed, provided stability conditions are met [21]. This scenario represents the case of constrained negative

stiffness (CNS), which is very useful for vibro-acoustic damping [29, 30]. CNS is a simplified representation of an inclusion with NS embedded in a positive stiffness matrix material.

2.3 Effective Medium Theory

Micromechanical effective medium theory (EMT) is a very general modeling approach for estimating quasi-static macroscale stiffness and loss behavior of viscoelastic composite materials when the mesoscale parameters are known [30]. Stiffness and loss behavior can be modeled using these traditionally static models under quasi-static loading conditions using standard techniques by employing the elastic-viscoelastic correspondence principal [31]. The principal states that the stiffness tensors of each constituent, $\mathbf{C}$, can be represented with complex valued entities: $\mathbf{C} = \mathbf{C}^{'} + j\mathbf{C}^{''} = \mathbf{C}^{'}(\mathbf{I} + j\boldsymbol{\eta})$. Here, $\mathbf{C}$ is the fourth order complex stiffness tensor consisting of storage, $\mathbf{C}^{'}$, and loss, $\mathbf{C}^{''}$, components, $\mathbf{I}$ is the identity tensor, and $\boldsymbol{\eta}$ is the loss factor tensor. Under this principal, the usual operations applicable to EMT hold as long as all constituents display linear behavior for the applied loads and all spatial fluctuation in the stress and strain fields are much larger than the smallest scale of interest. The meso $\rightarrow$ macro scale transition presented in this work employs classical EMT to approximate the macroscale stiffness and loss for a known mesoscopic parameter set. The parameters of interest are the linearized stiffness and loss of each constituent as well as the volume fraction, morphology, and orientation distribution of the NS inclusions. Developed in previous work, models for isotropic constituents with spherical inclusions have implemented Self-Consistent (SC), Generalized Self-Consistent (GSC), Differential Effective Medium (DEM), and Mori-Tanaka (MT) effective medium schemes for this purpose [27, 29, 30, 32]. Some of these approaches require implicit numerical schemes, but have been shown to provide

good estimates of the effective properties of composite materials at both low and high volume fraction of heterogeneities [30, 33].

2.4 Small-Scale Structures and Acoustic Metamaterials

One emerging area of study in the fields of electromagnetics and acoustics, known as metamaterials, provides a possible route to the production of NS inclusions with broadband performance. Acoustical metamaterials are defined as subwavelength structures that lead to notable changes in the macroscopic properties of the material in ways that are not achievable with natural materials [16]. The vast majority of acoustical metamaterials in the literature rely on subwavelength resonant behavior to achieve the desired macroscopic response. For example, Yang et al. [34] created acoustic metamaterials with a negative dynamic mass to reflect low frequency sound waves. By altering the inclusions, the metamaterial can be tuned for specific applications such as sound focusing [35] and cloaking [36]. The reliance on resonance to elicit a desired response, which is prevalent in metamaterial research, has two significant drawbacks. First, it restricts the utility of the material element to a narrow band of frequencies around that resonance. Second, resonant behavior can be significantly altered by the presence of internal losses thereby reducing or even eliminating the ability of the metamaterial to provide the desired performance. The metamaterial elements discussed in this work do not rely on resonant behavior and are therefore useful over a very broad range of frequencies. For this reason, constrained negative stiffness metamaterials could be potentially useful for transducer backings, anechoic coatings, vibration isolation treatments, and shock absorbing materials or structures.

2.5 Metamodeling

The multiscale design and simulation of an energy absorbing composite material with small-scale buckled elements presents a difficult design problem. Complicated finite element and analytical models at each scale require considerable computational resources. In design problems such as this, metamodels, also known as surrogate models, can be developed and employed to engineer optimized materials in a computationally-efficient manner (for example, see Box and Wilson [37] and Sachs et al. [38]). Metamodels are arbitrary functions fitted to training data points, and then evaluated over a range of input in order to generate predictions of the base model.

In general, metamodels have been shown to produce fast and accurate estimations when compared with computationally-expensive computer models [39]. Furthermore, metamodels allow for the material design modeling to be conducted in a single design software platform, such as MATLAB® [40, 41]. For example, training data can be generated by a limited number of computationally-intensive FEA simulations within a given range of system parameter values. Then, a metamodel can be trained and implemented in MATLAB®, which could readily link the other models and optimization routines in the design problem.

Backlund [42] examines an array of metamodeling techniques, such as: polynomial regression, multivariate adaptive splines, support vector regression, kriging, radial basis functions, and neural networks. Each of these methods have been studied and implemented extensively for a wide range of design problems. Design problems exhibit a range of characteristics such as modality, linearity, dimensionality and continuity, and different metamodeling approaches handle these design problem attributes differently (and with differing success). Kriging has been shown to have good per-

formance in moderate dimensional test problems [43], and has been selected as the metamodeling approach for this work.

2.6 Set-Based Design Strategy

Finally, the design of a composite material with extreme damping at the macroscale due to structural phenomena present at the microscale can be thought of as two completely distinct design efforts, corresponding with the two scale transition models. While there is a wide array of design approaches that could be considered for this problem, a set-based collaborative design effort could yield efficiencies in the overall design process. Set-based design was studied extensively due to Toyota car manufacturing adopting the process in the 1990s and realizing significant gains in virtually all metrics analyzed [44–46]. Three key components of the successful implementation of concurrent set-based design is highlighted by Sobek et al. [45]: (1) map the design space, (2) integrate by intersection, and (3) establish feasibility before commitment.

For the design problem at hand, establishing the design and performance spaces at the micro $\rightarrow$ meso scale transition model would reveal the attainable geometric configurations of the NS inclusion and their associated performance. The performance space from this level can be propagated forward as the design space input to the second distinct design level, the meso $\rightarrow$ macro scale transition model. The performance map can be established at this level, and would reflect not only the attainable and feasible designs, but the high performance designs as well. At this point, the design space is fully explored, leading to gains in efficiency in generating designs of energy absorbing systems. The work of Shahan and Seepersad [47] applies Bayesian classifiers towards set-based design and could be used to exploit this process.

Chapter 3

Multiscale Modeling

3.1 Overview

This chapter documents the development and results of a multiscale material model (MMM), which was created to estimate the elastic response of a continuous matrix material containing structured inclusions that demonstrate negative stiffness (NS) behavior. The model can be used for analysis and, by maintaining generality throughout each scale, it can also serve as a design tool enabling the generation of optimized microstructures and constituent materials based on the material properties desired at the macroscale. The latter case is the subject of Chapter 4.

The model development discussed in this chapter begins at the smallest length scale of interest to capture physical phenomena that can be used to amplify material losses and continues to the application scale. This begins in Sec. 3.2 which introduces a candidate NS inclusion. Then, the multiscale modeling approach is laid out in Sec. 3.3, including descriptions of key scales, scale transitions, and assumptions in the MMM. The micro $\rightarrow$ meso and meso $\rightarrow$ macro scale transition models are presented in Secs. 3.4 and 3.5, respectively.

3.2 Candidate Negative Stiffness Metamaterial Inclusion

The work presented here exploits the unique non-monotonic force-displacement nature of buckled systems to produce highly absorptive composite materials. Taking inspiration from a buckled beam system described in Chapter 2, Fig. 3.1 shows a

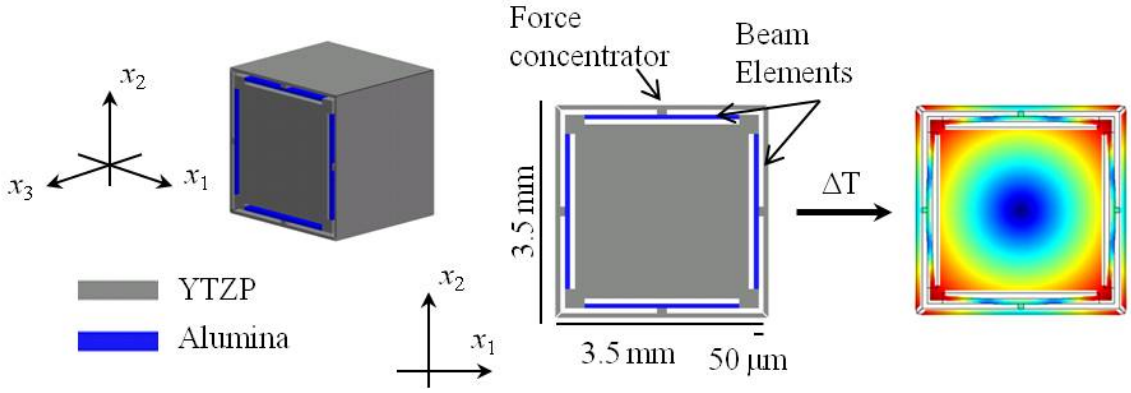

Figure 3.1: Mesoscale inclusion design for inducing NS in two orthogonal directions. The inclusion is assumed to be fabricated from YTZP and alumina materials. Thermal expansion mismatch and geometric symmetry can potentially induce buckling of the alumina elements.

metamaterial unit cell design, which consists of two constituent materials with different coefficients of thermal expansion, α, and the following elements: a supporting frame (high α), beams (low α), and "T"-shaped force concentrators (high α). Although the structure is composed of strictly linear elastic phases, nonlinear geometric loading produces structural bistability under specific thermo-mechanical fabrication conditions on four of the six faces. The structure therefore displays NS in two orthogonal directions. The force concentrators ensure that, once embedded, any force from the constraining matrix will be directed to the midpoint of the buckled beam element. Analysis has shown that without this element, the NS behavior of the inclusion can be reduced or eliminated.

A manufacturing technique known as micro co-extrusion is one potential fabrication process to create such elements because it has been proven capable of reliably producing complex small-scale structures with feature sizes as small as 5 μm and consisting of multiple materials [48–52]. Micro co-extrusion also incorporates a high temperature sintering step, which could potentially offer the thermal loading required to buckle components of the beam structure. To investigate the feasibility

of this approach for producing bistable inclusions, alumina (Al_2O_3, Young's modulus, Y=386 GPa, Poisson's ratio, ν=0.22, shear modulus, μ=158.2 GPa, α=8.1x10^{-6} K^{-1}) and yttria-stabilized tetragonal zirconia polycrystals (YTZP) (Y_2O_3, Y=210 GPa, ν=0.23, μ=85.4 GPa, α=10.3x10^{-6} K^{-1}) are the two ceramics that are considered due to availability for experimental evaluation. Future work could consider different materials that perhaps have a greater contrast in coefficients of thermal expansion.

3.3 Multiscale Modeling Approach

Figure 3.2 depicts a schematic of the multiscale modeling approach developed in this work. Models are developed that ultimately provide an estimation of the macroscopic stiffness and loss tensor of a composite material containing a small volume fraction of buckled metamaterial unit cells embedded in a linear viscoelastic matrix material. This is achieved using two separate scale transition models and considers constituent material properties at all scales, microscale geometry, metamaterial unit cell orientations, and the thermal load imposed to generate microscale buckling.

The micro $\rightarrow$ meso scale transition model is represented in Fig. 3.2 (a)–(b). It is an energy-based nonlinear homogenization model that employs finite element (FE) methods to calculate the strain energy of the metamaterial unit cell at constant temperature for a range of displacements imposed at the boundary of the cell and is unique to this work. This model captures the evolution of the strain energy as a function of imposed strain, and therefore provides estimates of the apparent nonlinearly evolving stiffness of the metamaterial units. The meso $\rightarrow$ macro scale transition model schematized in Fig. 3.2 (c)–(e), on the other hand, is a classical linear micromechanical homogenization model that employs the elastic-viscoelastic correspondence principal [53]. This model uses the leading order (linearized) mesoscale stiffness of the

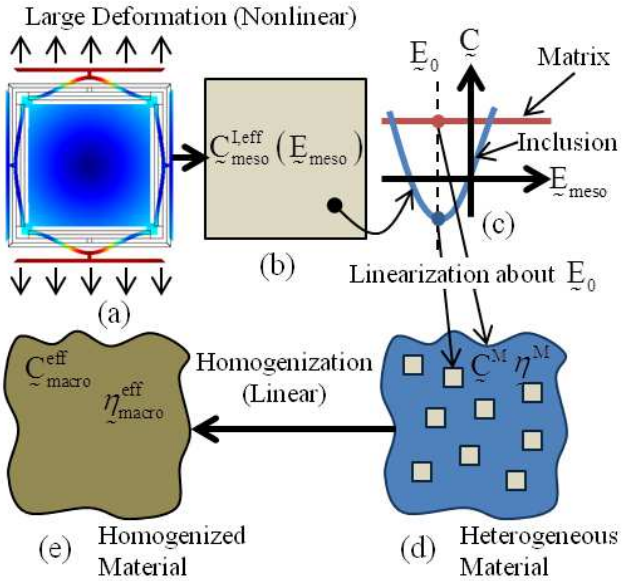

Figure 3.2: Schematic of the MMM developed in this work.

metamaterial cells at a strain state of interest and the linear stiffness and loss factor of the matrix material to provide an estimate of the local (i.e., tangent) stiffness and loss of the composite at the macroscale. A more detailed description of each of the models are presented in the following sections, but first, it is informative to describe the scales of interest in the MMM, and the approximations of the modeling approach that has been implemented.

3.3.1 Description of Scales, Scale Transitions, and the Small-on-Large Approximation

Figure 3.3 illustrates the various scales of interest in this work. The candidate inclusion design is shown in panel (a). The microscale, L_μ, is denoted by the length scale of the smallest design dimensions of the inclusion. Next, the mesoscale, L_m, is denoted by the length scale of the inclusion embedded in the matrix material, and shown in panel (b). Finally, the macroscale, L_M, is shown in panel (c) and denoted by the length scale of a volume of matrix material containing the inclusions that is

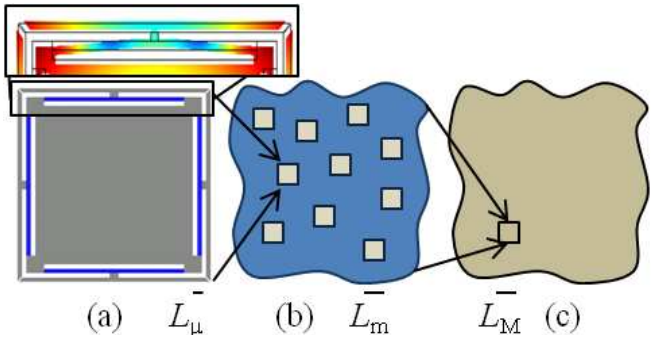

Figure 3.3: Depiction of scales and scale transitions in the MMM: (a) microscale, L_{μ} (thermally-induced buckling of top beam element depicted in inset); (b) mesoscale, L_{m}; and (c) macroscale, L_{M}.

assumed to represent the behavior of the homogenized composite.

As discussed above, The MMM consists of two scale transitions, schematized in Fig. 3.2: (*i*) the micro $\rightarrow$ meso and (*ii*) meso $\rightarrow$ macro. While the latter is derived from classical micromechanical effective medium theory (EMT), the former represents a unique scale transition model which considers large deformations of structured inclusions. These models are coupled together in a specific manner in order to capture the physical behavior that motivates this study: a composite material containing small scale NS elements to enhance vibro-acoustic damping capacity. While vibro-acoustic energy is associated with small oscillations about some equilibrium position, the mechanism used to generate NS (buckling of small scale elements) is associated with large microscopic deformations. The scale transition models have been implemented in a manner that captures this dichotomy. Specifically, the micro $\rightarrow$ meso scale transition captures the evolution of microscopic stiffness due to large strains imposed at the boundary of the metamaterial unit cells and the subsequent meso $\rightarrow$ macro scale transition captures the effects of small perturbations about an equilibrium position of interest.

This approach is highly analogous to the work of Cherkaoui et al. [54] In that

work, a nonlinear macroscopic stress-strain response of a metal-matrix composite containing phase-transforming shape memory alloy (SMA) inclusions was approximated using microscale evolution equations for the SMA response and a linear EMT to approximate the tangent modulus for small perturbations about an equilibrium position. More relevant to this study is the work of Parnell and co-workers [55, 56] who investigate the influence of a large pre-existing strain in the neighborhood of coated inclusions on elastic wave scattering. Both the present work and that of Parnell et al. attempt to model elastic wave phenomena known as 'small-on-large' behavior or the acoustoelastic effect. Most research on acoustoelasticity focuses on harmonic generation due to enhancement of higher order elastic constants due to elastic nonlinearity when a material is subjected to high stress levels [57]. The interest of this study, however, is the evolution of the *leading order* elastic constants of small-scale metamaterial heterogeneities and how they lead to drastic enhancement of the macroscopic loss factor of a composite containing nonlinear metamaterial unit cells. The details of these scale transition models are presented in Secs. 3.4 and 3.5.

3.4 Micro $\rightarrow$ Meso Scale Transition Model

The multiscale modeling approach starts at the microscale (i.e., the scale of important geometric features of the metamaterial inclusion) and effective nonlinear mesoscale stiffness of the NS inclusion. Consider the candidate inclusion design as depicted in Fig. 3.1, which is envisioned as being manufactured by micro co-extrusion. Inclusions manufactured using this process would undergo successive extrusions and a high-temperature sintering process to produce the desired microscale geometry. The sintering process provides the thermal loading required to induce NS behavior. In order to accurately estimate the inclusion stiffness, the method presented here allows for nonlinear mechanical behavior and considers the effects of thermal loading.

3.4.1 Hooke's Law and Anisotropic Elastic Constants

Hooke's Law relates the (Cauchy) stress, σ_{ij}, and strain, E_{kl}, of an elastic solid through a stiffness tensor (tacitly assumed to be linear in the following formulation), C_{ijkl}, and is defined by Eq. (3.1):

$$\sigma_{ij} = C_{ijkl} E_{kl}. \tag{3.1}$$

The term C_{ijkl} is a fourth-order tensor with a maximum of 21 independent constants needed to describe a fully anisotropic material due to symmetry conditions. The four subscripts of C_{ijkl} can therefore be reduced to two (C_{IJ}) using a contracted (also known as "Voigt") notation, where subscripts 1, 2, 3, 4, 5, and 6 denote 11, 22, 33, 23/32, 13/31, and 12/21, respectively. Thus, the general constitutive equation for a fully anisotropic material can be represented in matrix form as:

$$\begin{bmatrix} \sigma_1 \\ \sigma_2 \\ \sigma_3 \\ \sigma_4 \\ \sigma_5 \\ \sigma_6 \end{bmatrix} = \begin{bmatrix} C_{11} & C_{12} & \cdot & \cdot & \cdot & C_{16} \\ C_{21} & C_{22} & & & & \\ \cdot & & \cdot & & & \\ \cdot & & & \cdot & & \\ \cdot & & & & \cdot & \\ C_{61} & & & & & C_{66} \end{bmatrix} \begin{bmatrix} E_1 \\ E_2 \\ E_3 \\ E_4 \\ E_5 \\ E_6 \end{bmatrix}. \tag{3.2}$$

The candidate inclusion design possesses geometric symmetry such that the elastic response is identical in the x- and y-direction. This behavior is similar to materials with tetragonal symmetry, which are fully described by six independent constants [58]. The linearized elastic response of the candidate inclusion can therefore be represented with Eq. (3.3):

$$\begin{bmatrix} \sigma_1 \\ \sigma_2 \\ \sigma_3 \\ \sigma_4 \\ \sigma_5 \\ \sigma_6 \end{bmatrix} = \begin{bmatrix} C_{11} & C_{12} & C_{13} & 0 & 0 & 0 \\ C_{12} & C_{11} & C_{13} & 0 & 0 & 0 \\ C_{13} & C_{13} & C_{33} & 0 & 0 & 0 \\ 0 & 0 & 0 & C_{44} & 0 & 0 \\ 0 & 0 & 0 & 0 & C_{44} & 0 \\ 0 & 0 & 0 & 0 & 0 & C_{66} \end{bmatrix} \begin{bmatrix} E_1 \\ E_2 \\ E_3 \\ E_4 \\ E_5 \\ E_6 \end{bmatrix}. \tag{3.3}$$

The following sections present a method for estimating these elastic constants for a structured inclusion such as the one shown in Fig. 3.1 using FE methods.

3.4.2 Internal Energy and Stiffness

A critical step in the multiscale modeling process is to find a physically meaningful and accurate estimate of the effective stiffness of the metamaterial structures that display nonlinear behavior and NS. Recall that the features of these metamaterial elements are considered to be on the microscale while their overall dimensions define the mesoscale. Further, without approximating the structured inclusion as a continuous material with effective elastic properties, it is impossible to employ traditional EMT to perform the meso $\rightarrow$ macro scale transition step and estimate the macroscopic performance of a composite material containing these metamaterial elements. The structure depicted in Fig. 3.1 presents significant difficulties in this regard since its elastic response is anticipated to be anisotropic and nonlinear. Accordingly, the primary challenge addressed by this work is the development of a methodology for extracting the effective anisotropic stiffness of a structured inclusion that is robust to the effects of nonlinearities brought about by bistability induced by microscale geometry and element fabrication.

The method forwarded by this work is based on a power law approximation of the strain energy of a material system in terms of the applied strain field. The Cauchy stress, σ_{ij}, is defined as the change in specific internal energy, U, with respect to the applied strain field, E_{ij} [28]:

$$\frac{\partial U}{\partial E_{ij}} = \sigma_{ij}, \tag{3.4}$$

where E_{ij} is Green's strain tensor, given by:

$$E_{ij} = \frac{1}{2}\left(u_{i,j} + u_{j,i} + u_{k,i}u_{k,j}\right), \tag{3.5}$$

where a comma denotes a partial derivative with respect to a corresponding coordinate.

A general form of the internal energy (Helmholtz free energy) within a continuous medium as a function of strain at constant temperature is determined from the following summation [59]:

$$U\left(\underset{\approx}{E}\right) = U_0 + U^{\text{coupled}}\left(\underset{\approx}{E}\right) + U^{\text{elastic}}\left(\underset{\approx}{E}\right) + \cdots, \tag{3.6}$$

where $\underset{\approx}{E}$ denotes E_{ij}, U_0 is the undeformed internal energy, $U^{\text{coupled}}\left(\underset{\approx}{E}\right)$ is due to coupling from other domains (e.g., piezoelectricity), and $U^{\text{elastic}}\left(\underset{\approx}{E}\right)$ is due to elastic deformation. Equation (3.6) can therefore be approximated with a power law expansion on strain, as given by the expression:

$$U\left(\underset{\approx}{E}\right) = U_0 + B_{ij}E_{ij} + \frac{1}{2}C_{ijkl}E_{ij}E_{kl} + \frac{1}{6}D_{ijklmn}E_{ij}E_{kl}E_{mn} + \cdots, \tag{3.7}$$

where B_{ij}, C_{ijkl}, and D_{ijklmn} are tensors of increasing order relating a particular component strain energy to an imposed strain. Here B_{ij} is identified as a stress generated by coupled fields, $\sigma_{ij}^{\text{coupled}}$, and C_{ijkl}, D_{ijklmn}, $\cdots$, are elastic stiffness tensors of fourth and higher orders.

Thus, a general form of nonlinear stiffness, $C_{ijkl}^{\text{NL}}\left(\underset{\approx}{E}\right)$, that lumps all the higher order terms in Eq. (3.7) can be related to the elastic strain energy function:

$$C_{ijkl}^{\text{NL}}\left(\underset{\approx}{E}\right) = \frac{\partial^2 U^{\text{elastic}}\left(\underset{\approx}{E}\right)}{\partial E_{ij}\partial E_{kl}} = C_{ijkl} + D_{ijklmn}E_{mn} + \cdots. \tag{3.8}$$

Given this general relationship between stiffness and elastic strain energy, the following sections present a method for estimating strain energy in a material given an applied strain and extracting the components of $C_{ijkl}^{\text{NL}}\left(\underset{\approx}{E}\right)$ that are related to pure modes of deformation.

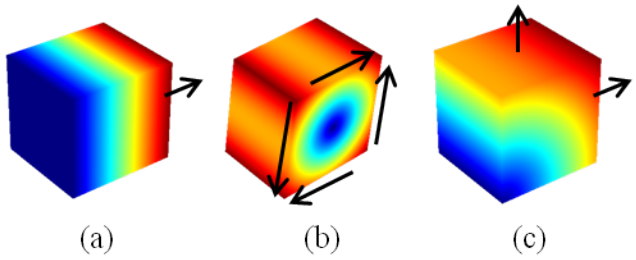

Figure 3.4: Example resulting deformations indicative of the direct energy method for determining (a) axial, (b) shear, and (c) off-diagonal elastic constants. Black arrows indicate direction of applied displacements.

3.4.3 Direct Energy Method

Odegard [60] employed what will be called a direct energy method to calculate the effective behavior of a representative volume element (RVE) of multiphase continuous piezoelectric materials using Finite Element Analysis (FEA). That method, which is generalized in 3.4.5, involves computing the change in internal energy within an RVE resulting from a single small displacement imposed on the boundary. Figure 3.4a–c shows example loading conditions for the determination of axial, shear, and off-diagonal stiffnesses, respectively, along with the resulting deformations when using the direct energy method.

For small deformations at the boundary of the RVE, B, the displacements, $u_i(B)$, can be related to the imposed strain, E_{ij}, and the dimension of an RVE cube, L^{m}, by $u_i(B) = E_{ij}L^{\mathrm{m}}\mathrm{n}_j$, where n is the unit normal vector of the RVE face where the displacement is imposed. Note that this formulation has made the assumption that the strain in the RVE is small. The resulting total elastic strain energy is then defined by the following relation:

$$U_{\mathrm{E}} = \sum_{m=1}^{n} U_{\mathrm{E}}^{m} = \frac{V_o}{2} C_{ijkl} E_{ij} E_{kl}, \tag{3.9}$$

where U_{E}^{m} is the elastic strain energy of element m, n is the total number of finite

elements constituting the RVE, and V_o is the initial volume of the RVE. Equation (3.9) can then be used to derive the stiffness values, C_{ijkl}, based on the applied strain, E_{ij}, as detailed in the Secs. 3.4.3.2–3.4.3.4.

3.4.3.1 A Note on 2D Plane Strain FEA

Equation (3.9) relates the strain energy of the volume, stiffness, and strain of a 3D RVE. The units of elastic strain energy, U_{E}, in Eq. (3.9) are $\mathrm{Pa} \cdot \mathrm{m}^3 = \mathrm{J}$. Oftentimes, full 3D FEA is not practical due to considerable computational time and resources required. Thus, a 2D approximation (either plane strain or plane stress) can be made which greatly reduces the time and computing power required to obtain a solution. During this work, a 2D plane strain FEA was performed on the RVE as needed. Note that under the 2D approximation, Eq. (3.9) takes the form:

$$U_{\mathrm{E}}^{\mathrm{2D}} = \sum_{m=1}^{n} U_{\mathrm{E}}^{m} = \frac{A_o}{2} C_{ijkl} E_{ij} E_{kl}, \tag{3.10}$$

where A_o is the initial in-plane area. The units of the 2D strain energy, $U_{\mathrm{E}}^{\mathrm{2D}}$, are $\mathrm{Pa} \cdot \mathrm{m}^2 = \mathrm{J/m}$.

3.4.3.2 Derivation of Axial Stiffness

For the axial stiffness case, as shown in Fig. 3.4a, the strain is applied in only one direction, x_1 for example, as described by Eq. (3.11):

$$E_{11} = E, \ \underset{\sim}{E} = 0 \text{ else.} \tag{3.11}$$

Equation (3.9) then becomes:

$$U_{\mathrm{E}} = \frac{V_o}{2} C_{1111} E_{11} E_{11} = \frac{V_o}{2} C_{11} \left(E\right)^2. \tag{3.12}$$

Rearranging Eq. (3.12), one obtains the following simple expression for C_{11}:

$$C_{11} = \frac{2U_{\mathrm{E}}}{V_o \left(E\right)^2}. \tag{3.13}$$

3.4.3.3 Derivation of Shear Stiffness

To determine the shear stiffness, C_{44} for example, as shown in Fig. 3.4b, the strain is applied in two counter-opposing directions, as described by Eq. (3.14):

$$E_{23} = E_{32} = E,\ \underset{\sim}{E} = 0 \text{ else.} \tag{3.14}$$

Equation (3.9) then becomes:

$$\begin{aligned} U_{\mathrm{E}} &= \frac{V_o}{2}\left[C_{2323}E_{23}E_{23} + C_{2332}E_{23}E_{32} + C_{3223}E_{32}E_{23} + C_{3232}E_{32}E_{32}\right] \\ &= \frac{V_o}{2}\left[4C_{44}\left(E\right)^2\right] = 2V_oC_{44}\left(E\right)^2. \end{aligned} \tag{3.15}$$

An expression for C_{44} can thus be obtained:

$$C_{44} = \frac{U_{\mathrm{E}}}{2V_o\left(E\right)^2}. \tag{3.16}$$

3.4.3.4 Derivation of Off-Diagonal Stiffness

Finally, determination of the off-diagonal terms, such as C_{12}, as shown in Fig. 3.4c, result from strain applied in two orthogonal directions, as described by Eq. (3.17):

$$E_{11} = E_{22} = E,\ \underset{\sim}{E} = 0 \text{ else.} \tag{3.17}$$

Equation (3.9) then becomes:

$$\begin{aligned} U_{\mathrm{E}} &= \frac{V_o}{2}\left[C_{1111}E_{11}E_{11} + C_{1122}E_{11}E_{22} + C_{2211}E_{22}E_{11} + C_{2222}E_{22}E_{22}\right] \\ &= \frac{V_o}{2}\left(E\right)^2\left[C_{11} + 2C_{12} + C_{22}\right]. \end{aligned} \tag{3.18}$$

An expression for C_{12} can thus be obtained:

$$C_{12} = \frac{U_{\mathrm{E}}}{V_o\left(E\right)^2} - \frac{\left(C_{11} + C_{22}\right)}{2}, \tag{3.19}$$

where C_{11} and C_{22} are obtained from Eq. (3.13).

After Odegard [60], Table 3.1 summarizes the relations for obtaining all six independent constants using the direct energy approach.

Table 3.1: Summary of the displacements and expressions to determine the independent constants of a tetragonally-symmetric medium using the direct energy approach [60].

Property	Applied Strain	Displacements	Elastic Energy
C_{11}	$E_{11} = E,\ \underset{\sim}{E} = 0$ else	$u_1(B) = EL^{\mathrm{m}}\mathrm{n}_1$ $u_2(B) = 0$ $u_3(B) = 0$	$U_{\mathrm{E}} = \frac{V}{2} C_{11} (E)^2$
C_{33}	$E_{33} = E,\ \underset{\sim}{E} = 0$ else	$u_1(B) = 0$ $u_2(B) = 0$ $u_3(B) = EL^{\mathrm{m}}\mathrm{n}_3$	$U_{\mathrm{E}} = \frac{V}{2} C_{33} (E)^2$
C_{44}	$E_{23} = E_{32} = E,\ \underset{\sim}{E} = 0$ else	$u_1(B) = 0$ $u_2(B) = EL^{\mathrm{m}}\mathrm{n}_3$ $u_3(B) = EL^{\mathrm{m}}\mathrm{n}_2$	$U_{\mathrm{E}} = 2VC_{44} (E)^2$
C_{66}	$E_{12} = E_{21} = E,\ \underset{\sim}{E} = 0$ else	$u_1(B) = EL^{\mathrm{m}}\mathrm{n}_2$ $u_2(B) = EL^{\mathrm{m}}\mathrm{n}_1$ $u_3(B) = 0$	$U_{\mathrm{E}} = 2VC_{66} (E)^2$
C_{12}	$E_{11} = E_{22} = E,\ \underset{\sim}{E} = 0$ else	$u_1(B) = EL^{\mathrm{m}}\mathrm{n}_1$ $u_2(B) = EL^{\mathrm{m}}\mathrm{n}_2$ $u_3(B) = 0$	$U_{\mathrm{E}} = \frac{V(E)^2}{2} [C_{11} + C_{22} + 2C_{12}]$
C_{13}	$E_{11} = E_{33} = E,\ \underset{\sim}{E} = 0$ else	$u_1(B) = EL^{\mathrm{m}}\mathrm{n}_1$ $u_2(B) = 0$ $u_3(B) = EL^{\mathrm{m}}\mathrm{n}_3$	$U_{\mathrm{E}} = \frac{V(E)^2}{2} [C_{11} + C_{33} + 2C_{13}]$

Table 3.2: Results of 2D plane strain direct energy method benchmark.

	Strain Energy Density [J/m]	Stiffness Formula	Calculated Stiffness [GPa]	Benchmark Stiffness Formula	Benchmark Stiffness [GPa]
C_{11}	1482	$\frac{2U_{\mathrm{E}}}{A_o(E)^2}$	296.3	$\frac{Y(1-\nu)}{(1+\nu)(1-2\nu)}$	296.3
C_{22}	1482	$\frac{2U_{\mathrm{E}}}{A_o(E)^2}$	296.3	$\frac{Y(1-\nu)}{(1+\nu)(1-2\nu)}$	296.3
C_{12}	4423	$\frac{U_{\mathrm{E}}}{A_o(E)^2} - \frac{(C_{11}+C_{22})}{2}$	146.0	$\frac{E(\nu)}{(1+\nu)(1-2\nu)}$	146.0
C_{66}	1504	$\frac{U_{\mathrm{E}}}{2A_o(E)^2}$	75.2	$\frac{Y}{2(1+\nu)}$	75.2

3.4.4 Benchmarking the Direct Energy Approach

In order to benchmark the direct energy approach, two separate models were developed in COMSOL Multiphysics®: (*i*) a 2D plane strain and (*ii*) a full 3D model. For each of these models, the RVE consisted of a block of steel (Y = 200 GPa, $\nu = 0.33$) with an in-plane cross-sectional area, A_0, of 1 x 1 m, and an out of plane depth of 1 m. Displacements were applied to the steel RVE as per Table 3.1 for a strain value, E, of 1x10^{-4}. The results from the 2D plane strain benchmark are displayed in Table 3.2, and the 3D benchmark results are displayed in Table 3.3. In each case, the results from the direct energy method are equal to the values calculated from the benchmark stiffness formulas. This particular implementation of the direct energy method is thus validated.

3.4.5 Energy Derivative Method

A similar approach, referred to in this work as the energy derivative method, can be implemented that is better suited for nonlinear elastic behavior. Like the direct energy approach, the energy derivative method also applies prescribed strains on the surface of the RVE and calculates the resulting strain energy. The primary difference is that the energy derivative method requires the calculation of strain energy for a

Table 3.3: Results of 3D direct energy method benchmark.

	Strain Energy Density [J/m]	Stiffness Formula	Calculated Stiffness [GPa]	Benchmark Stiffness Formula	Benchmark Stiffness [GPa]
C_{11}	1482	$\frac{2U_{\mathrm{E}}}{V_o(E)^2}$	296.3	$\frac{Y(1-\nu)}{(1+\nu)(1-2\nu)}$	296.3
C_{22}	1482	$\frac{2U_{\mathrm{E}}}{V_o(E)^2}$	296.3	$\frac{Y(1-\nu)}{(1+\nu)(1-2\nu)}$	296.3
C_{33}	1482	$\frac{2U_{\mathrm{E}}}{V_o(E)^2}$	296.3	$\frac{Y(1-\nu)}{(1+\nu)(1-2\nu)}$	296.3
C_{12}	4423	$\frac{U_{\mathrm{E}}}{V_o(E)^2} - \frac{(C_{11}+C_{22})}{2}$	146.0	$\frac{Y(\nu)}{(1+\nu)(1-2\nu)}$	146.0
C_{23}	4423	$\frac{U_{\mathrm{E}}}{V_o(E)^2} - \frac{(C_{22}+C_{33})}{2}$	146.0	$\frac{Y(\nu)}{(1+\nu)(1-2\nu)}$	146.0
C_{13}	4423	$\frac{U_{\mathrm{E}}}{V_o(E)^2} - \frac{(C_{11}+C_{33})}{2}$	146.0	$\frac{Y(\nu)}{(1+\nu)(1-2\nu)}$	146.0
C_{44}	1504	$\frac{U_{\mathrm{E}}}{2V_o(E)^2}$	75.2	$\frac{Y}{2(1+\nu)}$	75.2
C_{55}	1504	$\frac{U_{\mathrm{E}}}{2V_o(E)^2}$	75.2	$\frac{Y}{2(1+\nu)}$	75.2
C_{66}	1504	$\frac{U_{\mathrm{E}}}{2V_o(E)^2}$	75.2	$\frac{Y}{2(1+\nu)}$	75.2

range of imposed deformations. Once the resulting strain energies are calculated, the local, or tangent, stiffness of the element at a specified strain state can be calculated directly from the local curvature of the strain energy versus strain plot. This approach has the distinct advantage that it is ambivalent with regard to the linearity of the stress-strain relation, can take into account finite deformations, and can be used to find higher order elastic constants (though the latter is not considered in this work). The energy derivative method is therefore a robust approach for determining the stiffness of materials and microstructure whose constitutive elastic response evolves nonlinearly when large strains are imposed at its boundaries.

The basic premise, as shown in Eq. (3.8), is that a strain-dependent nonlinear local stiffness tensor of a material can be obtained by taking the second partial derivative of the strain energy function with respect to the imposed strain. For the case when U_{E} is determined through FEA, as is the current case, those derivatives are found numerically. A formula relating stiffness, strain energy, and strain can therefore

be derived for each of stiffness values using the curvature of the strain energy function for the element of interest.

3.4.5.1 Derivation of Axial Stiffness

Starting with Eq. (3.12), but replacing C_{11} with $C_{11}^{\mathrm{NL}}\left(\underset{\sim}{E}\right)$, the stress function is obtained from the first partial derivative of the strain energy function with respect to strain:

$$\sigma_{ij}\left(\underset{\sim}{E}\right) = \frac{\partial U_{\mathrm{E}}\left(\underset{\sim}{E}\right)}{\partial E} = V\left(\underset{\sim}{E}\right) C_{11}^{\mathrm{NL}}\left(\underset{\sim}{E}\right) E, \tag{3.20}$$

where $V\left(\underset{\sim}{E}\right)$ represents the current volume, as opposed to the initial reference volume, V_o, in the direct energy approach. The stiffness is then obtained by taking the second partial derivative of the strain energy function with respect to the imposed strain to yield:

$$C_{11}^{\mathrm{NL}}\left(\underset{\sim}{E}\right) = \frac{1}{V\left(\underset{\sim}{E}\right)} \frac{\partial^2 U_{\mathrm{E}}\left(\underset{\sim}{E}\right)}{\partial \left(E\right)^2}. \tag{3.21}$$

3.4.5.2 Derivation of Shear Stiffness

Starting with Eq. (3.15), but replacing C_{44} with $C_{44}^{\mathrm{NL}}\left(\underset{\sim}{E}\right)$, the stress function is obtained from the first partial derivative of the strain energy function with respect to strain:

$$\sigma_{ij}\left(\underset{\sim}{E}\right) = \frac{\partial U_{\mathrm{E}}\left(\underset{\sim}{E}\right)}{\partial E} = 4V\left(\underset{\sim}{E}\right) C_{44}^{\mathrm{NL}}\left(\underset{\sim}{E}\right) E. \tag{3.22}$$

The stiffness is then obtained by taking the second partial derivative of the strain energy function with respect to the imposed strain to yield:

$$C_{44}^{\mathrm{NL}}\left(\underset{\sim}{E}\right) = \frac{1}{4V\left(\underset{\sim}{E}\right)} \frac{\partial^2 U_{\mathrm{E}}\left(\underset{\sim}{E}\right)}{\partial \left(E\right)^2}. \tag{3.23}$$

3.4.5.3 Derivation of Off-Diagonal Stiffness

Starting with Eq. (3.18), but replacing C_{11}, C_{12}, and C_{22} with associated nonlinear representations, the stress function is obtained from the first partial derivative of the strain energy function with respect to strain:

$$\sigma_{ij}\left(\underset{\approx}{E}\right) = \frac{\partial U_{\mathrm{E}}\left(\underset{\approx}{E}\right)}{\partial E} = V\left(\underset{\approx}{E}\right) E\left[C_{11}^{\mathrm{NL}}\left(\underset{\approx}{E}\right) + C_{22}^{\mathrm{NL}}\left(\underset{\approx}{E}\right) + 2C_{12}^{\mathrm{NL}}\left(\underset{\approx}{E}\right)\right]. \tag{3.24}$$

The stiffness is then obtained by taking the second partial derivative of the strain energy function with respect to the imposed strain to yield:

$$C_{12}^{\mathrm{NL}}\left(\underset{\approx}{E}\right) = \frac{1}{2}\left[\frac{1}{V\left(\underset{\approx}{E}\right)}\frac{\partial^2 U_{\mathrm{E}}\left(\underset{\approx}{E}\right)}{\partial\left(E\right)^2} - \left(C_{11}^{\mathrm{NL}}\left(\underset{\approx}{E}\right) + C_{22}^{\mathrm{NL}}\left(\underset{\approx}{E}\right)\right)\right]. \tag{3.25}$$

Table 3.4 captures the energy derivative method formulas and boundary conditions required for the determination of the six independent elastic constants of the candidate inclusion geometry. This method is employed to calculate the effective mesoscopic stiffness of a candidate microstructure. First, calculations of given isotropic elastic constants were performed in order to benchmark the method, as shown in Sec. 3.4.6.

3.4.6 Benchmarking the Energy Derivative Method

A cube of isotropic steel ($Y = 200$ GPa, $\nu = 0.33$) is used to benchmark the energy derivative method. After applying a range of displacements to the front yz-face in the x-direction, the resulting strain energy plot is shown in Fig. 3.5a. Figure 3.5a depicts the smooth parabolic form of the strain energy as a function of engineering strain. Taking the first derivative of the strain energy function with respect to the applied displacement yields the stress function, depicted in Fig. 3.5b, which illustrates how the stress function follows a linear form with constant slope and y-intercept of 0. Finally, taking the second partial derivative of the strain energy function with respect

Table 3.4: Summary of the displacements and expressions to determine the independent constants of an tetragonally-symmetric medium using the energy derivative approach.

Property	Applied Strain	Derivative Method Stiffness
C_{11}	$E_{11} = E,\ \underline{E} = 0$ else	$C_{11}^{\mathrm{NL}}(\underline{E}) = \frac{1}{V(\underline{E})}\frac{\partial^2 U_{\mathrm{E}}(\underline{E})}{\partial (E)^2}$
C_{33}	$E_{33} = E,\ \underline{E} = 0$ else	$C_{33}^{\mathrm{NL}}(\underline{E}) = \frac{1}{V(\underline{E})}\frac{\partial^2 U_{\mathrm{E}}(\underline{E})}{\partial (E)^2}$
C_{44}	$E_{23} = E_{32} = E,\ \underline{E} = 0$ else	$C_{44}^{\mathrm{NL}}(\underline{E}) = \frac{1}{4V(\underline{E})}\frac{\partial^2 U_{\mathrm{E}}(\underline{E})}{\partial (E)^2}$
C_{66}	$E_{12} = E_{21} = E,\ \underline{E} = 0$ else	$C_{66}^{\mathrm{NL}}(\underline{E}) = \frac{1}{4V(\underline{E})}\frac{\partial^2 U_{\mathrm{E}}(\underline{E})}{\partial (E)^2}$
C_{12}	$E_{11} = E_{22} = E,\ \underline{E} = 0$ else	$C_{12}^{\mathrm{NL}}(\underline{E}) = \frac{1}{2}\left[\frac{1}{V(\underline{E})}\frac{\partial^2 U_{\mathrm{E}}(\underline{E})}{\partial (E)^2} - \left(C_{11}^{\mathrm{NL}}(\underline{E}) + C_{22}^{\mathrm{NL}}(\underline{E})\right)\right]$
C_{13}	$E_{11} = E_{33} = E,\ \underline{E} = 0$ else	$C_{13}^{\mathrm{NL}}(\underline{E}) = \frac{1}{2}\left[\frac{1}{V(\underline{E})}\frac{\partial^2 U_{\mathrm{E}}(\underline{E})}{\partial (E)^2} - \left(C_{11}^{\mathrm{NL}}(\underline{E}) + C_{33}^{\mathrm{NL}}(\underline{E})\right)\right]$

to applied displacement yields the stiffness. As indicated in Fig. 3.5c, this value is equal to 296 GPa for all displacements, which is equal to the known value of C_{11} for isotropic steel, as given by Eq. (3.26):

$$C_{11} = \frac{Y(1-\nu)}{(1+\nu)(1-2\nu)} = \frac{200\text{ GPa}\,(0.67)}{(1.33)(0.34)} = 296\text{ GPa}. \tag{3.26}$$

To stress the point, this example illustrates that for linear elastic materials, the strain energy function assumes a parabolic form; the stress function is a monotonically-increasing line with constant slope; and the stiffness is a line of constant value across all applied displacements. This example demonstrates why applying a single small strain, as in the direct energy approach, is sufficient for characterizing linear elastic materials. Further, this shows how the energy derivative method is well suited as a more general method for determining elastic constants because there is no implicit assumption as to the linearity of the elastic response of the material.

Having presented a robust and benchmarked approach for estimating elastic constants (whether linear or not), this method can be applied to estimating the

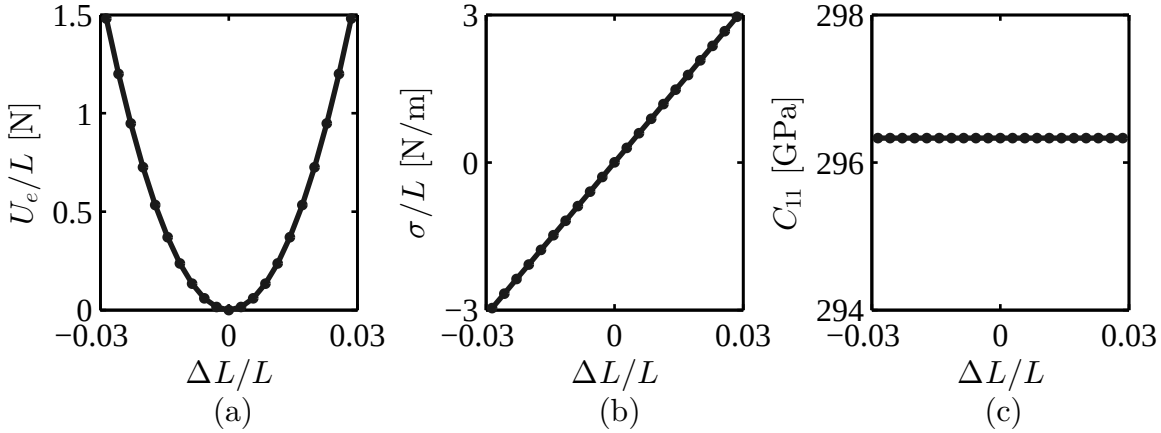

Figure 3.5: Benchmark results of energy derivative method for a cube of isotropic steel: (a) strain energy vs. engineering strain; (b) stress function vs. engineering strain; and (c) stiffness vs. engineering strain.

nonlinear elastic constants for a structured inclusion that employs a difference in coefficient thermal expansion to induce buckling behavior, as explored in Sec. 3.4.7.

3.4.7 Determination of Temperature-Dependent Stiffness Moduli

Characterization of the temperature-dependent effective elastic constants of structured inclusions like the one shown in Fig. 3.1 requires the implementation of a multistep FEA study that considers both the thermal and mechanical deformation. This work presents results of a two-step process implemented in COMSOL Multiphysics®. The first step solves the free thermal deformation for a given temperature change. An example deformation is shown in Fig. 3.6a. The thermal deformation is monitored at the external boundaries of the inclusion, and is considered the "zero" position for imposing the displacements listed in Table 3.4 in the second step.

The second step then simultaneously solves for the thermal deformation and the prescribed strain as outlined in Table 3.4 in order to determine each independent elastic constant of the mesoscale inclusion. An example deformation including

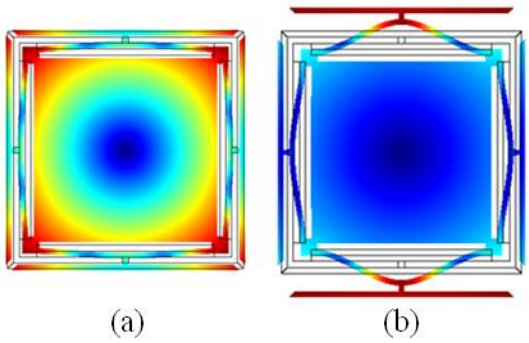

Figure 3.6: Representation of the (a) first step in multistep FEA analysis: example deformation of candidate inclusion after a change in temperature representative of manufacturing processing (note the web elements buckled outward); and (b) second step in multistep FEA analysis: example deformation of candidate inclusion subjected to a simultaneous change in temperature and mechanical loading.

thermal and mechanical loading is shown in Fig. 3.6b. In order to examine the effect of processing temperature on the inclusion stiffness values, a 2D plane strain FEA (energy derivative method) was performed on the candidate inclusion for varying temperatures.

3.4.7.1 Temperature-Dependent Strain Energy: C_{11} Loading

Examining the temperature-dependent strain energy in the case of C_{11} loading sheds significant insight on the effects of processing temperature on the inclusion. Figure 3.7 presents the temperature-dependent strain energy curves for a range of ΔT. While the curves appear to be linear, this is simply due to scaling; and the more interesting features of each strain energy curve become apparent in subsequent plots. From a zoomed-out perspective, Fig. 3.7 clearly demonstrates that an increase in ΔT results in an increase in U_{E}, due to the thermally-induced strain produced by thermal contraction of the inclusion.

If the inclusion did not possess beam elements capable of buckling, the curves in Fig. 3.7 would demonstrate the thermally-induced "DC offset" due to thermal

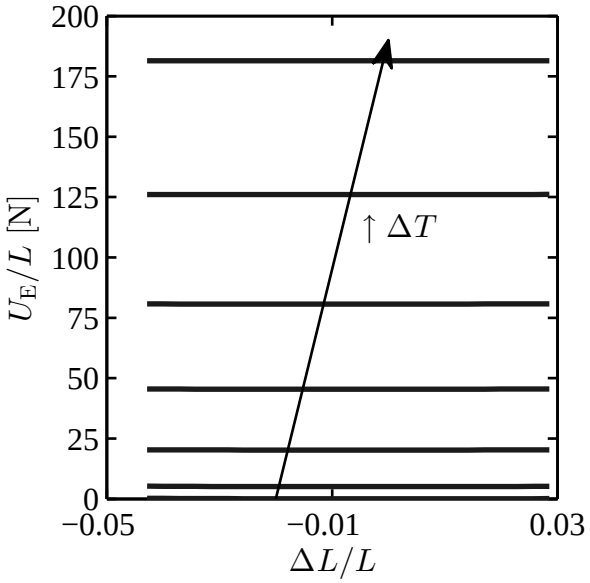

Figure 3.7: Temperature-dependent strain energy values over a range of engineering strains for ΔT values ranging from 0–1200 K in increments of 200 K. Arrow indicates increasing ΔT.

contraction, and little else. However, Fig. 3.8 highlights the interesting physics of the inclusion for three particular ΔTs. Figure 3.8a displays the strain energy curve of the inclusion for a ΔT of 0 K. This curve is relatively parabolic, and reminiscent of the strain energy curve of the benchmark model shown in Fig. 3.5a. As the ΔT is increased to 600 K, the strain energy curve shown in Fig. 3.8b begins to flatten out over a range of displacements. Recalling that the definition of stiffness is equal to the local curvature of the strain energy curve, Fig. 3.8b indicates the inclusion possesses nearly zero stiffness over a range of displacements equivalent to strain values of approximately -0.02 to 0.005. Finally, as the ΔT is increased to 1200 K, the strain energy curve shown in Fig. 3.8c clearly demonstrates two distinct energy wells. The existence of these energy wells confirms that the inclusion possesses NS for this particular processing temperature.

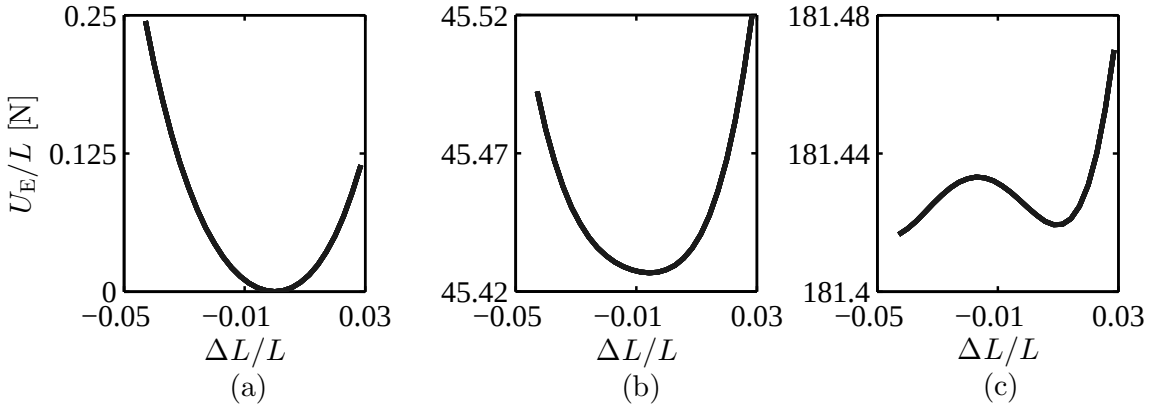

Figure 3.8: Strain energy vs. engineering strain of candidate inclusion under C_{11} loading for ΔT of: (a) 0 K; (b) 600 K; and (c) 1200 K.

3.4.7.2 Temperature-Dependent Stiffness Results

The resulting nonlinear temperature-dependent effective C_{11}, C_{12}, and C_{66} stiffnesses for a range of displacements and processing temperatures are presented in Fig. 3.9. Panels (a) and (b) of Fig. 3.9 clearly show that under certain thermo-mechanical loading, the beam elements undergo buckling and the effective stiffness of the inclusion is accordingly negative for a range of displacements. These results validate the approach of exploiting a coefficient of thermal expansion mismatch to obtain a NS inclusion. Figure 3.9c illustrates a very interesting temperature dependence of the shear stiffness (C_{66}) value. This is undoubtedly due to the relatively small contact area between the web and force-concentrating interface elements of the inclusion. These results further demonstrate the robustness of the energy derivative method and its ability to estimate nonlinear elastic responses.

3.4.8 Model Results of Candidate Inclusion

The preceding section provided the temperature-dependent stiffness values of the candidate inclusion in the plane where the most interesting physics (i.e., NS) reside. 2D FEA was sufficient to obtain these parameters, but a full 3D FEA was

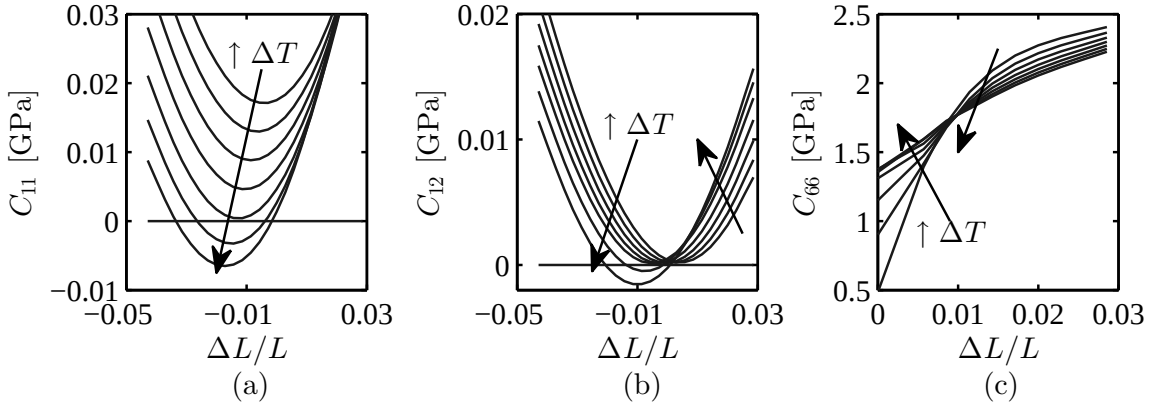

Figure 3.9: Temperature-dependent stiffness moduli vs. engineering strain of candidate microstructure for ΔT values ranging from 0–1200 K in increments of 200 K: (a) effective C_{11}; (b) effective C_{12}; and (c) effective C_{66} (note: change in x-axis made due to symmetry of response). Arrows indicate increasing values of ΔT.

Table 3.5: Strain energy and stiffness in a candidate structured inclusion using the direct FEA micro → meso scale transition model, for an applied strain, E, of 1x10^{-4}.

	C_{13}	C_{33}	C_{44}
Strain Energy Function (J)	3.96x10^{-6}	3.96x10^{-6}	2.54x10^{-7}
Stiffness (Pa)	4.28x10^{6}	2.26x10^{11}	3.62x10^{9}

required for the out of plane deformation (i.e., in the x_3-direction). The effective mesoscale stiffness results for the suite of applied displacements at the boundaries of the inclusion per the direct energy method are given in Table 3.5.

In order to integrate the nonlinear temperature-dependent outputs from the micro → meso scale transition model in subsequent modeling steps, they are linearized about the point of maximum NS, and combined with the linear 3D FEA results, presented in Eq. (3.27) as an effective mesoscopic stiffness tensor for the candidate inclusion at a representative manufacturing temperature ($\Delta T = 1200K$) (values in

MPa):

$$C_{IJ} = \begin{bmatrix} -6.53 & -0.85 & 4.28 & 0 & 0 & 0 \\ -0.85 & -6.53 & 4.28 & 0 & 0 & 0 \\ 4.28 & 4.28 & 2.26\text{x}10^5 & 0 & 0 & 0 \\ 0 & 0 & 0 & 3620 & 0 & 0 \\ 0 & 0 & 0 & 0 & 3620 & 0 \\ 0 & 0 & 0 & 0 & 0 & 1950 \end{bmatrix}. \tag{3.27}$$

These stiffness values are then used as inputs for the meso $\rightarrow$ macro scale transition model presented in Sec. 3.5.

3.5 Meso $\rightarrow$ Macro Scale Transition Model

3.5.1 Effective Medium Theory

A robust mesoscale to macroscale homogenization model is the only model that remains to complete the multiscale model of the structured lossy composite material proposed in this work. An anisotropic self-consistent (SC) EMT is employed for this purpose. The model takes the matrix stiffness tensor, the volume fraction, shape and orientation of the inclusions, and the effective mesoscopic stiffness tensor of the inclusion as inputs and calculates the effective macroscopic stiffness. This work employs a three-phase coated inclusion SC micromechanical model for coated ellipsoidal inclusions embedded in a continuous matrix which was developed in previous work [30, 32, 61]. These works employ Eshelby's assumption that the strain in the heterogeneities is spatially uniform at scales analogous to the mesoscale presented here [62].

The model is derived by first calculating the stress and strain fields in and around a coated inhomogeneity due to a macroscopically applied load in a process known as localization. Expressions for the effective viscoelastic properties are then determined in a process known as homogenization which finds weighted volumetric averages of the localized stress and strain fields resulting from the anisotropic vis-

coelastic contrast, the geometry, the orientation distribution, and the concentration of microscale inclusions. The model has been shown to provide a good approximation of the overall viscoelastic response of a composite medium under static and quasi-static dynamic loading scenarios through application of the elastic-viscoelastic correspondence principal [30, 32, 53].

The effective (complex valued) stiffness tensor of a composite containing coated inclusions are computed using Eqs. (3.28)–(3.32). In general, the SC model can be well understood as an intelligently weighted rule of mixtures approximation shown in Eq. (3.28):

$$C^{\text{eff}}_{ijkl} = C^{\text{M}}_{ijkl} + f^{\text{I}} \left[C^{\text{I}}_{ijmn} - C^{\text{eff}}_{ijmn} \right] A^{\text{I}}_{mnkl} + f^{\text{C}} \left[C^{\text{C}}_{ijmn} - C^{\text{eff}}_{ijmn} \right] A^{\text{C}}_{mnkl}. \tag{3.28}$$

In this expression the stiffness tensors, $\mathbf{C}^{\text{X}}$, of each material are denoted with an $M; I;$ or C superscript to represent the matrix, inclusion or coating, respectively, and the tensors $\mathbf{A}^{\text{I}}$ and $\mathbf{A}^{\text{C}}$ represent quantities known as strain localization tensors for the inclusion and coating phases, respectively. The strain localization tensors relate the macroscopic strain, $\varepsilon^{\text{g}}_{ij}$, to the average inclusion (or coating) strain, $\bar{\varepsilon}^{\text{I}}_{ij}$, through the relation:

$$\bar{\varepsilon}^{\text{I}}_{ij} = A^{\text{I}}_{ijkl} \varepsilon^{\text{g}}_{kl}. \tag{3.29}$$

For the current problem, the volume fraction of coating material is set equal to zero, $f^{\text{C}} = 0$, leaving only the volume fraction of inclusion, f^{I}, to influence the overall properties. The strain localization tensors represent tensorial intelligent weighting parameters and have significant influence on the effective properties calculated. They take into account not only the material anisotropy of each constituent phase, but also the inclusion form. For this work, only spherical inclusion geometry is considered for simplicity, however, wide ranges of inclusion geometries can be represented, ranging

from needle-like to penny-shaped. For the special case of an anisotropic matrix and inclusion with no coating, the inclusion strain localization tensor reduces to:

$$A^{\mathrm{I}}_{ijkl} = \left[I_{ijkl} + T^{\mathrm{I}}_{ijmn}\left(C^{\mathrm{eff}}_{ijkl}\right)\left(C^{\mathrm{I}}_{mnkl} - C^{\mathrm{eff}}_{mnkl}\right)\right]^{-1}. \tag{3.30}$$

where $I_{ijkl} \equiv \mathbf{I}_4$ is the fourth order identity tensor and $\mathbf{T}^{\mathrm{I}}\left(\mathbf{C}^{\mathrm{eff}}\right)$ is the volume average of the volume integral of the second order spatial derivative of the Green's tensor, $G^{\mathrm{eff}}_{ij}\left(\mathbf{r}-\mathbf{r}'\right)$:

$$T^{\mathrm{I}}_{ijkl}\left(C^{\mathrm{eff}}_{ijkl}\right) = \frac{1}{V^{\mathrm{I}}}\int_{V^{\mathrm{I}}}\int_{V^{\mathrm{I}}} -\frac{1}{2}\left[G^{\mathrm{eff}}_{ik,jl}\left(\mathbf{r}-\mathbf{r}'\right) + G^{\mathrm{eff}}_{jk,il}\left(\mathbf{r}-\mathbf{r}'\right)\right]. \tag{3.31}$$

In Eq. (3.31), V^{I} represents the volume of the inclusion, and the Green's tensor, $G^{\mathrm{eff}}_{ij}\left(\mathbf{r}-\mathbf{r}'\right)$, calculates the displacement in i-direction at the point $\mathbf{r}$ in the effective medium due to a unit force in the j-direction resulting from an inhomogeneity located at point $\mathbf{r}'$. $G^{\mathrm{eff}}_{ij}\left(\mathbf{r}-\mathbf{r}'\right)$ is defined as the tensor that satisfies the differential equation:

$$C^{\mathrm{eff}}_{ijkl}G^{\mathrm{eff}}_{km,lj}\left(\mathbf{r}-\mathbf{r}'\right) + \delta_{im}\delta\left(\mathbf{r}-\mathbf{r}'\right) = 0. \tag{3.32}$$

Full evaluation of Eq. (3.31) is a non-trivial task and details of the Fourier transform technique for obtaining an approximate solution can be found in Berveiller et al. [63] and the appendix of Haberman [27]. Furthermore, inspection of Eq. (3.30) shows that the SC model is implicit and numerical methods are required for its implementation. Despite these complexities, it is known to provide very accurate solutions for a wide range of problems [30], so its use has been employed as the meso $\rightarrow$ macro scale transition model in this work.

3.5.2 Validating Mesoscale Homogenization Approach

The multiscale modeling approach has assumed that the nonlinear stress and strain behavior resulting from the inclusion structure and thermal processing can be

well represented as a continuous elastic solid domain with nonlinear effective elastic properties at the mesoscale, $\mathbf{C}^{\text{eff}}_{\text{meso}}(\mathbf{E}_{\text{meso}})$, where $\mathbf{C}^{\text{eff}}_{\text{meso}}$ is the effective nonlinear mesoscopic stiffness tensor and $\mathbf{E}_{\text{meso}}$ is the Green's strain tensor evaluated at the mesoscale. The advantage of this assumption is that it permits the use of the homogenized mesoscopic stiffness tensor as a strain-dependent input to classic micromechanical meso $\rightarrow$ macro scale transition models. To validate this assumption and benchmark the unique hybrid FEA and analytical multiscale modeling approach described here, the three different cases outlined below and schematized in Fig. 3.10 were considered for determining the effective macroscopic stiffness tensor, $\mathbf{C}^{\text{eff}}_{\text{macro}}$, of a composite consisting of a matrix containing a known volume fraction of structured inclusions:

1. Three different micromechanical effective medium models of a matrix containing homogeneous linear elastic spherical particulate inclusions. The models used here are the Differential Effective Medium (DEM), the Self-Consistent (SC), and the Mori-Tanaka (MT) models;

2. FEA of an RVE consisting of a matrix containing a homogeneous cubic inclusion with known elastic properties; and

3. FEA of an RVE consisting of a matrix containing a structured inclusion with the geometry shown in Fig. 3.1. This represents an FEA of all scales present and no scale transition approximations.

The resulting effective macroscopic stiffness values from these three different cases are compared for a range of inclusion volume fractions in Fig. 3.11.

The mesoscopic inclusion stiffness, $\mathbf{C}^{\text{eff}}_{\text{meso}}$, which is an input to model sets 1 and 2, was found using the direct energy method on the structured inclusion to

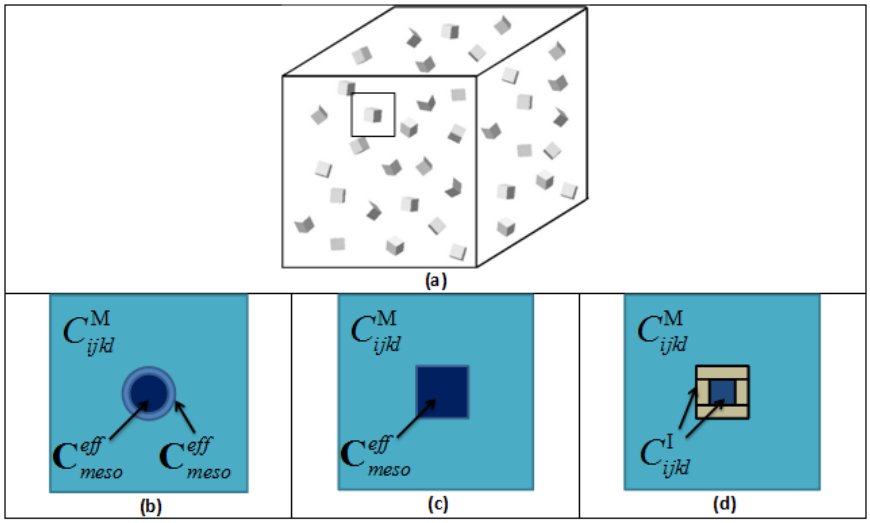

Figure 3.10: Three multiscale modeling validations of increasing complexity. (a) shows a conceptual image of a certain volume fraction of inclusions dispersed throughout a continuous matrix material, (b) depicts the composition and geometry used associated with analytical modeling, (c) shows the geometry and properties used in FEA effective medium models, and (d) depicts the geometry and properties employed doing a single-step multiscale FEA approximation model.

determine its small strain (linearized) stiffness tensor. It is important to stress that this step for model set 1 mimics the approach that is advocated in this work for nonlinear inclusion behavior and is therefore highly relevant to the validation of the multiscale modeling approach. For all modeling sets, the scale transition modeling was performed with an isotropic matrix material have a Young's modulus, Y, of 1 GPa and a Poisson's ratio, ν, of 0.3. Compositions having volume fraction (in percent) of $\phi \in \left[\begin{array}{cccccc} 0.1 & 1 & 2 & 3 & \ldots & 10 \end{array} \right]$ were considered here as low inclusion concentrations are of interest. The results from each of the models are shown in Fig. 3.11.

These results show that there is good agreement between the various modeling approaches for determining effective macroscopic stiffness properties. It is worth noting that the three analytical EMT models produce essentially the same values for all inclusion volume fractions at these concentration levels and that both sets of FE

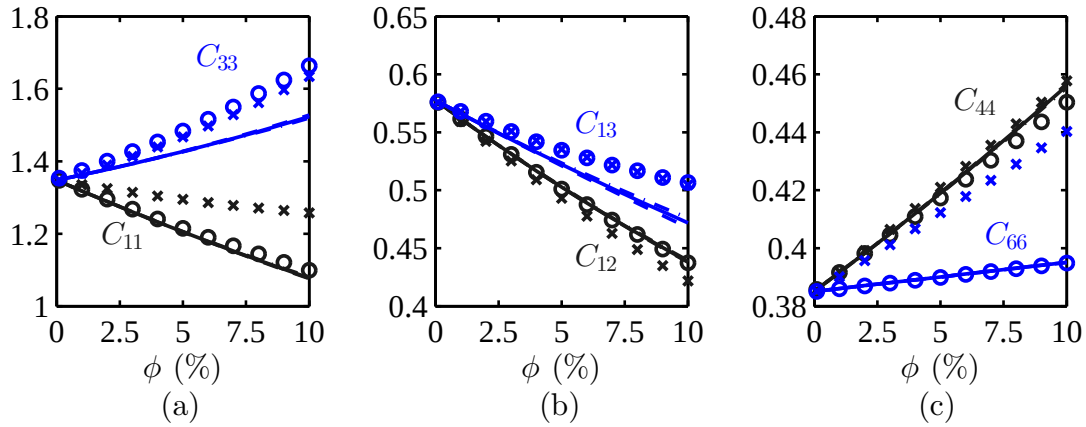

Figure 3.11: Effective stiffness values verses volume fraction: (a) axial stiffness: black – C_{11}, blue – C_{33}; (b) off-diagonal stiffness: black – C_{12}, blue – C_{12}; and (c) shear stiffness: black – C_{44}, blue – C_{66}. Solid line = differential effective medium; dashed line = generalized self-consistent model; dashed line with dots = Mori-Tananka; FEA with $\mathbf{C}^{\mathrm{I}} = \mathbf{C}^{\mathrm{eff}}_{\mathrm{meso}}$ denoted by an 'o'; and FEA with structured inclusion with $\mathbf{C}^{\mathrm{I}}$ denoted by an 'x'.

models closely follow these trends. At the elevated volume fraction of 10%, the FEA-structured inclusion case differs from the EMT results by no more than 20%, which is a reasonable error level [64]. For the purposes of this research, where volume fractions of interest are limited approximately 2%, the results of the EMT and FEA approaches are in very good agreement. Therefore the micro $\rightarrow$ meso scale transition approach employed in this research captures the physics dominating the influence of microscale structure on the effective properties at the macroscale. Given the good agreement between stiffness values and general trending among all models, the assumption that the stress-strain state of a structured inclusion can be well represented by a solid inclusion of bulk anisotropic properties is thus considered validated and of utility for multiscale modeling and design purposes. It is acknowledged, however, that the level of discrepancy is higher than desired for highly accurate multiscale modeling, specifically with respect to the effective shear moduli of the composite, which should be addressed in future research.

3.5.3 Model Results

Using the results of the FEA presented in Section 3.4.8 as the effective stiffness of the mesoscopic inclusion, Fig. 3.12 shows the effective properties calculated for a composite containing 2% by volume of identically-oriented microstructured NS inclusions with the properties given in Eq. (3.27). The matrix material was assumed to be isotropic was varied such that the ratio, $C_{11}^{\mathrm{I}}/\mathbb{R}\left[C_{11}^{\mathrm{M}}\right] \in \begin{bmatrix}-1.5 & -0.25\end{bmatrix}$. The matrix was assumed to have a small loss factor, η^{M}, of 0.05 and a Poisson's ratio, ν^{M}, of 0.30. The results present the overall properties normalized by the properties of the matrix for a wide range of possible inclusion to matrix stiffnesses. The objective in making these plots is to determine what ratio of negative inclusion stiffness to matrix stiffness provides the desired overall performance. Inspection of the resulting effective anisotropic properties clearly shows that drastic changes in overall stiffness and loss factor occur for stiffness ratios of approximately $C_{11}^{\mathrm{I}}/\mathbb{R}\left[C_{11}^{\mathrm{M}}\right] \in \begin{bmatrix}-1.25 & -0.75\end{bmatrix}$. The largest predicted increase occurs for the stiffness components oriented in the x_1- (and by symmetry, the y_1-) direction: $C_{11}^{\mathrm{eff}} = C_{22}^{\mathrm{eff}}$, C_{12}^{eff} and $C_{13}^{\mathrm{eff}} = C_{23}^{\mathrm{eff}}$. The off-diagonal component, C_{12}^{eff}, produces a maximum loss factor ratio of $\approx 20\eta^{\mathrm{M}}$, whereas C_{11}^{eff} and C_{13}^{eff} each produce maximum loss factor ratios $\approx 10\eta^{\mathrm{M}}$. It's worth noting that these plots indicate that it is possible to simultaneously increase both the stiffness and loss of a composite compared to the matrix material with the addition of a very small amount of constrained NS inclusions. Furthermore, these results suggest that viscoelastic materials containing even very low volume fractions of inclusions structured as shown in Fig. 3.1 will display drastic increases in energy absorption while the change in overall stiffness can be tuned based on the ratio of the inclusion to matrix stiffness.

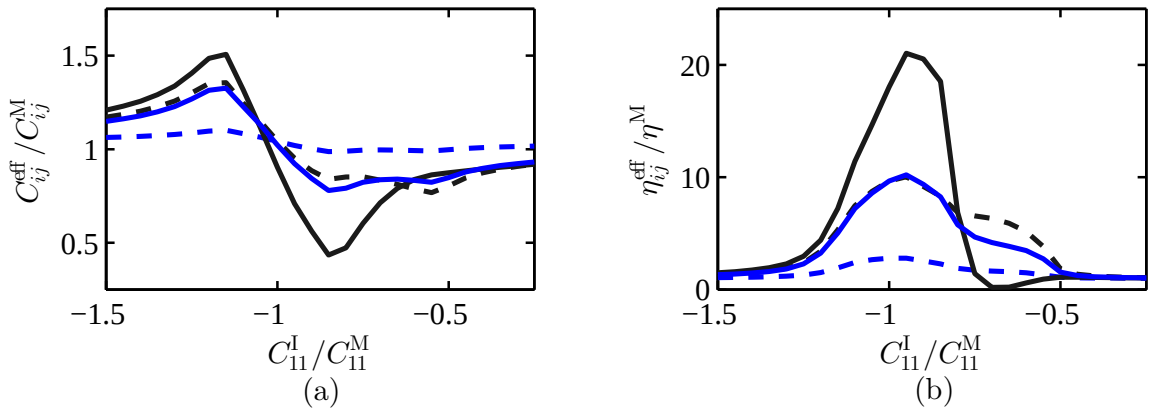

Figure 3.12: Effective stiffness and loss properties predicted by the Self-Consistent model for a composite containing identically-oriented 2% by volume of the mesoscale inclusions. The matrix is assumed to have $\nu = 0.30$ and $\eta = 0.05$. Stiffness and loss values ($*$ denotes complex-valued) for $C_{11}^{\text{eff}^*}$ – dashed black line; $C_{12}^{\text{eff}^*}$ – solid black line; $C_{33}^{\text{eff}^*}$ – dashed blue line; and $C_{13}^{\text{eff}^*}$ – solid blue line.

3.6 Summary and Conclusions

The results presented in this chapter were achieved through a combination of finite element and analytical multiscale material models for specific structures designed to exhibit NS. The results indicate that structures displaying NS behavior can indeed be designed using buckled elements. Further, a very general finite element energy based approach has been derived, implemented, and benchmarked to determine the nonlinear effective stiffness of a structured element. This unique approach can now be harnessed as a powerful tool for the future design of engineered microstructure to elicit non-intuitive macroscopic behavior, as demonstrated in Chapter 4. Furthermore, since this approach does not target resonant behavior (as is the case in the vast majority of metamaterial approaches), NS structures produced using this approach will be useful over a wide frequency bandwidth for energy absorption. While the EMT model used in this work is essentially a quasi-static model, these results consider dynamic effects (1) within the material through viscoelastic losses and (2) within the inclusion. These results work under the assumption that the inclusions

are much smaller than the the wavelength of excitation. As such, the fields within the inclusion are considered uniform. These results can be considered valid for excitation frequencies where wave phenomena can be neglected. Given these underlying assumptions, this multiscale modeling approach provides a powerful tool in the design of microstructured composite materials.

Chapter 4

Hierarchical Design of Composite Materials with Negative Stiffness Inclusions

4.1 Overview

The chapter utilizes the mulitscale material model (MMM) presented in Chapter 3 to examine the characteristics of thermal expansion mismatch microscale inclusions over a wide range of geometric parameters by means of a surrogate model of geometry-dependent stiffness. Design and performance mappings of the micro $\rightarrow$ meso scale transition are presented in Sec. 4.3 and the meso $\rightarrow$ macro scale transition is explored in Sec. 4.4. Finally, a composite beam with a high loss coating is used to demonstrate how the approach in this chapter can yield highly optimized results in Sec. 4.5.

4.2 Introduction

The design of composite materials with microscale, negative stiffness (NS) inclusions is challenging from several perspectives. First, the design space is complex. The MMM introduced in Chapter 3 must consider the geometry and material properties of the microstructure as well as the volume fraction, morphology, and orientation distribution of the inclusions at the mesoscale. The relationships between these variables are sometimes highly nonlinear. Furthermore, computationally expensive finite element (FE) methods are required to model the constitutive mesoscale properties of the inclusion, and these models are difficult to automate. Similarly, due to im-

plicit numerical solution techniques, micromechanical effective medium approaches for modeling the meso → macro scale transition can display numerical instability, which prevents full automation of the design exploration process. In addition, the design space includes discrete variables, such as alternative topologies of the inclusions, and highly nonlinear relationships between the geometric characteristics of those inclusions and the macroscopic loss behavior. Uncertainty also plays an important role, for example, in the impact of process-induced variations in the geometry of inclusions on their mesoscale behavior. Though this variation is not explored here, it is a nontrivial component of the design of these types of materials and the modeling and design strategy must therefore be of appropriate generality to consider fabrication. All of these characteristics, plus the inherently multilevel nature of the design problem, motivate the need for a comprehensive approach for multilevel design of these material systems. This approach is the topic of the current chapter.

4.3 The Micro → Meso Scale Transition Model Design Space

Figure 4.1 illustrates the modeling approach implemented in this section, beginning with the parameterization of the inclusion geometry and ending with the mesoscale design space exploration. In the micro → meso scale model, the geometries of the inclusions are designed to provide NS in at least one direction. The parameterization of a candidate inclusion and the homogenization approach for predicting its properties are described in Sec. 4.3.1. Section 4.3.2 then introduces the concept of geometry-dependent stiffness and Sec. 4.3.3 describes the development of a surrogate model to estimate the stiffness for a wide range of geometry parameters. This is followed by Sec. 4.3.4 which provides a validation of the surrogate model. Finally, mappings of the design and performance spaces are described in Sec. 4.3.5.

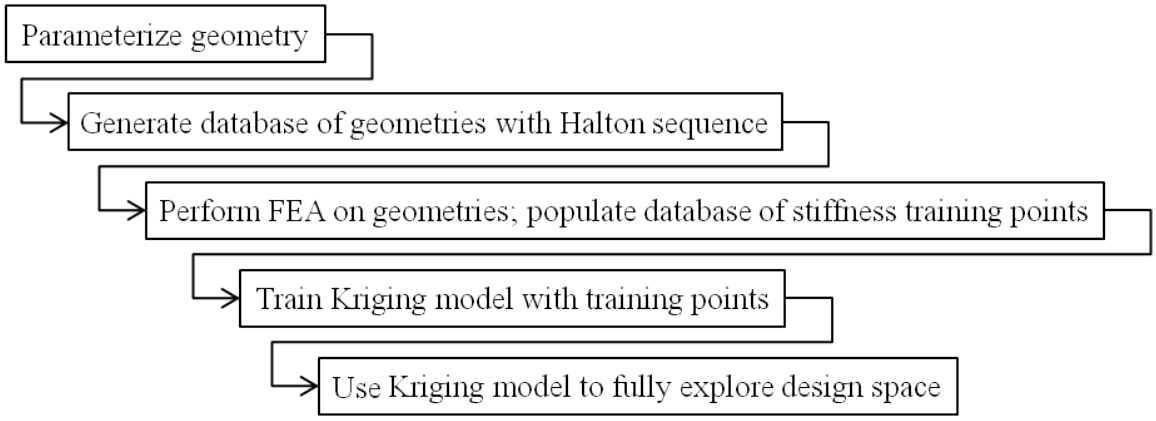

Figure 4.1: Schematic of modeling approach developed to explore the mesoscale design space.

4.3.1 Layout and Modeling of the Negative Stiffness Inclusions

A candidate geometry for the NS inclusion is depicted in Fig. 4.2. The inclusion is intended to be manufactured using a micro co-extrusion process, in which successive extrusions of a green part reduce the inclusion's external and internal dimensions from millimeter to micrometer scale [48–52]. During the extrusion process, voids are filled with a carbon black material. Post-extrusion, a high-temperature sintering process pyrolizes the carbon black from the extrudate, which leaves voids within the inclusion. The inclusion is comprised of two materials, alumina (Al_2O_3) and yttria tetragonal zirconia polycrystals (YTZP), whose coefficients of thermal expansion differ. Given the temperature change experienced during sintering and cool-down to room temperature, differential contraction during the sintering process axially compresses the four alumina beams in Fig. 4.2 so that they assume the outwardly buckled, bistable states depicted on the right of Fig. 4.2. When the inclusion is embedded in a matrix material and mechanically loaded, NS of the inclusion can be induced, leading to greater localized strains, and hence greater stiffness and damping, than positive stiffness inclusions.

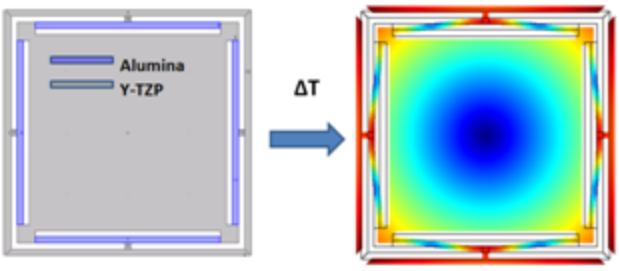

Figure 4.2: A candidate inclusion design showing FE modeling.

Figure 4.3 illustrates the geometric parameters that define the inclusion. The external boundary of the inclusion, and the mesoscale, is defined by the parameter L. The parameter $2H$ defines the height of a "T"-shaped interface which transfers loading from the constraining matrix to the buckled element. The parameter T defines the width of the connection between the interface and the buckled element. The parameter L_1 locates the midpoint of the inclusion, $L_1 = L/2 - 2H$. The parameter B defines the height of the buckled element and the voided region below it. Finally, L_2 defines the length of the element that will buckle by design. To reduce the dimensionality of the problem, non-dimensional ratios are used to adjust the inclusion geometry. The ratios of interest are $R_{L_1L_2}$, R_B, and R_{L_2T}, as defined by Eq. (4.1):

$$R_{L_1L_2} = \frac{L_2}{L_1};\ R_B = \frac{2B}{(L_1 - L_2)};\ \text{and}\ R_{L_2T} = \frac{T}{L_2}. \tag{4.1}$$

To relate the geometric parameters of the inclusion to the effective elastic properties of the inclusion, a two-step, nonlinear, multi-scale material homogenization method is applied to the inclusion, as detailed in Chapter 3. In that multiscale model, nonlinear finite element analysis (FEA) is used to obtain the strain energy of the inclusion for a range of displacements and boundary conditions, from which the leading order elasticity constants are determined. The nonlinear FE model considers

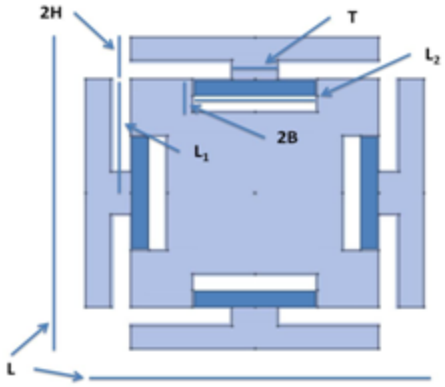

Figure 4.3: Cross-section view of parameterized inclusion geometry with all critical parameters. YTZP shown in light blue; alumina elements in dark blue.

both the geometric nonlinearity of the inclusion structure and the loading induced by differential thermal contraction during the sintering process. The methodology then assumes that the nonlinear stress and strain behavior resulting from the inclusion structure can be well-represented as a continuous elastic solid inclusion with nonlinear mesoscopic effective elastic properties, $\mathbf{C}^{\mathrm{m,eff}}(\mathbf{E}^{\mathrm{m}})$, where $\mathbf{C}^{\mathrm{m,eff}}$ is the effective nonlinear mesoscopic stiffness tensor and $\mathbf{E}^{\mathrm{m}}$ is the Green's strain tensor evaluated at the boundaries of the inclusion. Elements of the effective nonlinear mesoscopic stiffness tensor are calculated from the curvature of the inclusion's strain energy versus Green's strain relationship, using energy methods, as fully described in Chapter 3. The mesoscopic stiffness tensor is then used as a strain-dependent input to the meso $\rightarrow$ macro scale transition model in Sec. 4.4.

4.3.2 Microstructural Design: Geometry-Dependent Stiffness

In order to provide a full inspection of the design space for this particular inclusion geometrical framework, a range of values for each geometric ratio was established and particular geometries were constructed using a Halton sequence [65]. A Halton sequence is a deterministic sequencing approach based on a prime number

Table 4.1: Range of values.

Ratio	Min	Max
$R_{L_1L_2}$	0.6	0.99
R_B	0.1	0.98
R_{L_2T}	0.05	0.2

base. The Halton sequence offers a means to produce quasi-random sampling of a wide design space, and allows one to easily add permutations to the dataset, provided that the ranges of parameters to be inspected remain constant. The dataset presented here consisted of 1,000 geometries sampled from the ranges for each ratio specified in Table 4.1. These ranges were chosen to provide a broad sampling range resulting in both negative and positive values of effective mesoscopic stiffness.

Using COMSOL® LiveLink™ for MATLAB®, two different FEA studies were implemented. Each study contained an automated inclusion geometry construction and meshing routine. The first study analyzed the nonlinear 2D plane strain temperature dependent elasticity constants C_{11}, C_{12}, and C_{66} over a range of imposed displacements. The second study analyzed the linear 3D elasticity constants, C_{11}, C_{12}, C_{13}, C_{33}, C_{44}, and C_{66}. Figure 4.4 shows 8 example geometric configurations with associated FEA meshes intended to show the wide range of tested geometries.

This FEA data, which altogether amounted to over 500,000 data points, was used to build a metamodel of the geometric-dependent stiffness for each stiffness constant. A metamodel, or surrogate model, refers to a function fitted to arbitrary data points in order to save time and computational expense. While there are many approaches to generating metamodels, the approach used in this work is known as Kriging [38], and is explained in Sec. 4.3.3.

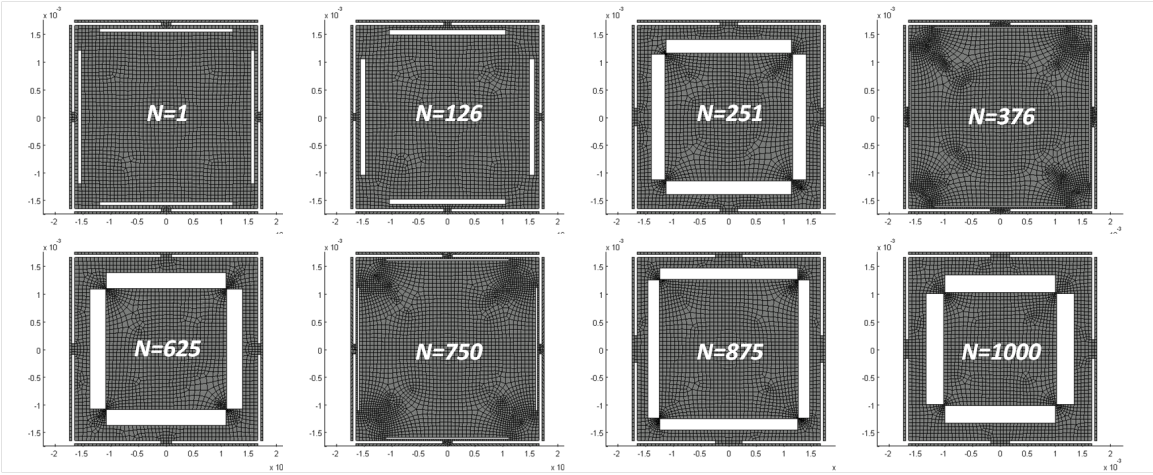

Figure 4.4: Example geometries generated by the Halton sequence.

4.3.3 Microstructural Design: Kriging Surrogate Modeling

Kriging builds a model based on a known global function with additional departures from the base model, as shown in Eq. (4.2):

$$y\left(x\right) = \sum_{j=1}^{k} \beta_i f_i\left(x\right) + Z\left(x\right), \tag{4.2}$$

where β_i are unknown coefficients and $f_i\left(x\right)$ are pre-defined functions. As Backlund et al. [66] point out, $Z\left(x\right)$ provides the departures from the base function in order to interpolate the training points, and is the realization of a stochastic process with a mean of zero, variance of σ^2, and nonzero covariance of the form:

$$\mathrm{cov}\left[Z\left(x_i\right), Z\left(x_j\right)\right] = \sigma^2 R\left(x_i, x_j\right), \tag{4.3}$$

where R is the user-specified correlation function. Similarly to Backlund et al. [66], a constant term for $f\left(x\right)$ is used in this study and a Gaussian curve is used for the correlation function that takes the form:

$$R\left(x_i, x_j\right) = \exp\left[-\theta_i (x_i - x_j)^2\right], \tag{4.4}$$

where θ_i are unknown correlation parameters that are automatically determined during the model fitting process. Although Kriging has been shown to be slow in terms

of build and prediction time compared with other metamodeling techniques [67], Kim et al. [43] demonstrate the ability of Kriging to successfully model nonlinear and multimodal problems. For this reason, Kriging was selected for generating a metamodel of inclusion stiffness in this work.

In general terms, surrogate models were developed for this project using a Kriging approach in order to determine the effective nonlinear mesoscopic stiffness as a function of inclusion geometry, constituent material properties, and thermomechanical loading. This can be stated in a pseudo-mathematical representation, shown in Eq. (4.5):

$$\mathbf{C}^{\mathrm{m,eff}} = f\left(\text{geometry},\ \text{materials},\ \text{displacement},\ \Delta T\right). \tag{4.5}$$

The advantage of this functional approach is that the effective mesoscopic stiffness can be calculated using an analytical function rather than a computationally expensive FE model. This is a powerful tool for the current material design problem because it permits the estimation of the mesoscale inclusion stiffness for any arbitrary geometry (within the provided bounds) in a matter of seconds as opposed to the hours required to generate results using computationally-intensive FE methods. It is important to note, however that one must generate a large dataset using FEA results in order to produce the surrogate model. Thus, a very general approach to obtaining accurate estimates of inclusion stiffness based on arbitrary geometries has been established and leveraged in this work to generate significant computational capabilities for a highly nonlinear constitutive microscale geometry that can be exploited to produce NS behavior. This will greatly enhance the future design of multiscale materials that employ microscale structure to generate NS behavior.

4.3.4 Kriging Model Validation

In order to validate the surrogate model developed in this work, the master dataset of 1,000 trials for each stiffness constant was used in two ways. First, roughly 10% of the dataset was used as "known" values, against which the predicted response of the mode was compared. Secondly, of the remaining 90% of the dataset, the model was trained using a certain number of training points, ranging from 10% to 100%, in increments of 10%. The error metrics used in this work follow analysis by Backlund et al. [42], namely the relative average absolute error (RAAE) and the relative maximum absolute error (RMAE). The RAAE is given by Eq. (4.6):

$$RAAE = \frac{\sum_{i=1}^{n} |y_i - \hat{y}_i|}{n\sigma}, \tag{4.6}$$

where y_i is the actual value of the base model at the i^{th} test point, $\hat{y}_i$ is the predicted value from the metamodel, n is the number of test cases, and σ is the standard deviation of the dataset used for training the model. The RMAE is given by Eq. (4.7):

$$RMAE = \frac{\max |y_i - \hat{y}_i|}{\sigma}, i = 1, \ldots, n. \tag{4.7}$$

This work also calculates and reports the average and maximum error without normalizing by the standard deviation. The average absolute error (AAE) is given by Eq. (4.8):

$$AAE = \frac{\sum_{i=1}^{n} |y_i - \hat{y}_i|}{n}. \tag{4.8}$$

The maximum absolute error (MAE) is given by Eq. (4.9):

$$MAE = \max |y_i - \hat{y}_i|, i = 1, \ldots, n. \tag{4.9}$$

The results of this validation are presented in Figs. 4.5–4.6. Figure 4.5 depicts the absolute (panel (a)) and relative (panel (b)) error metrics, respectively, for the 2D

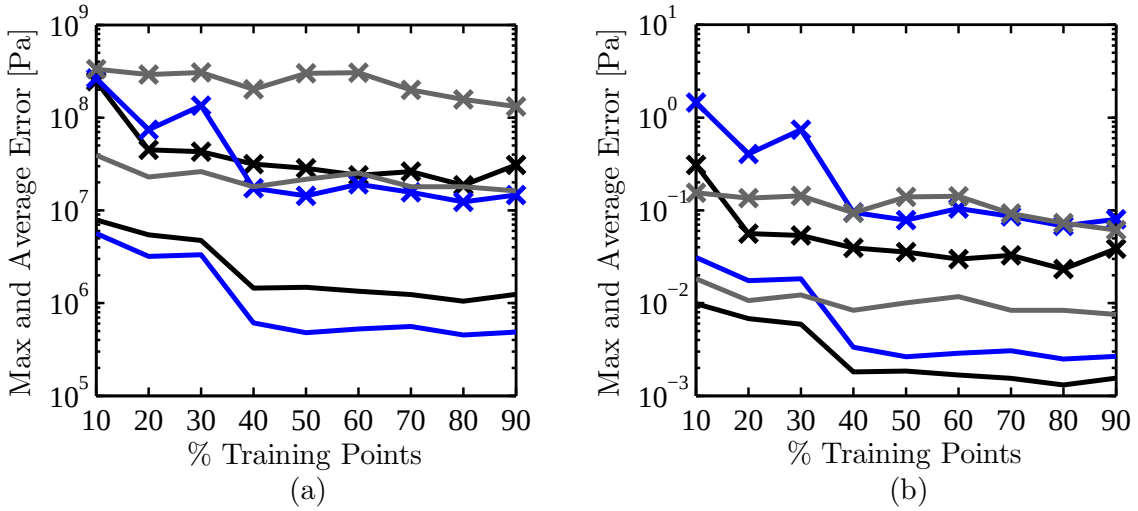

Figure 4.5: Error metrics for 2D stiffness values: (a) absolute and (b) relative error. Maximum values denoted by an 'x'. C_{11} error–solid black line, C_{12}–blue, and C_{66}–gray.

elastic constant (C_{11}, C_{12}, and C_{66}) trials; Fig. 4.6 depicts the error metrics for the 3D trials. Figures 4.5–4.6 demonstrate similar trends throughout the cross validation. While the maximum error in both 2D and 3D cases can be high (up to 1 GPa), when this error is normalized by the standard deviation of the dataset, the relative error decreases to 0.1, and even as low as 0.001, which indicates good performance of the model. Further, the results demonstrate that the model in each case asymptotically approaches a minimum error value when trained by at least 40% (approximately 400 test cases) of the master dataset. For the results presented in subsequent sections of this work, the model was trained by 100% of the dataset, so this validation yields high confidence in the accuracy of the surrogate model developed and employed in this work.

Having validated the Kriging model used to generate stiffness values over a wide range of geometries, Sec. 4.3.5 presents results of the micro $\rightarrow$ meso scale transition design space.

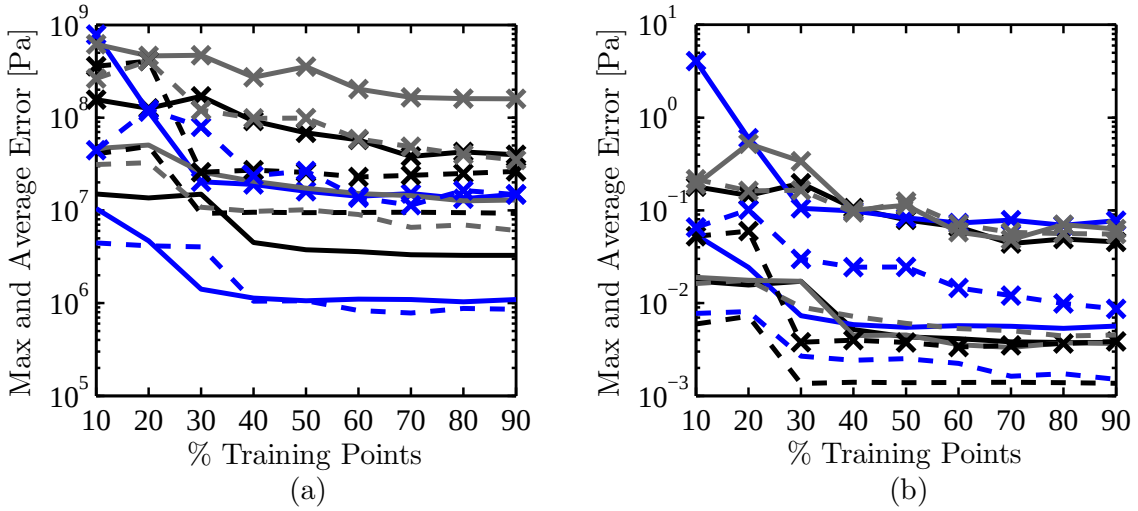

Figure 4.6: Error metrics for 3D stiffness values: (a) absolute and (b) relative error. Maximum values denoted by an 'x'. C_{11} error–solid black, C_{12}–solid blue, C_{66}–solid gray, C_{33}–dashed black line, C_{13}–dashed blue, and C_{44}–dashed gray.

4.3.5 Mapping the Micro → Meso Scale Transition Design Space

The micro → meso scale transition model design problem has three design variables, corresponding to the dimensionless parameters in Eq. (4.1), and six performance parameters, corresponding to elements of the mesoscopic effective stiffness tensor, $\mathbf{C}^{\mathrm{m,eff}}$. The performance parameters of particular interest in this example are two of the elements of the stiffness tensor, $C_{11}^{\mathrm{m,eff}}$ and $C_{12}^{\mathrm{m,eff}}$, which are directly related to the plane-strain bulk modulus of the inclusions. Values of the performance parameters are divided into two classifications. The high performance class captures designs that exhibit NS in the first principal direction: a negative value for $C_{11}^{\mathrm{m,eff}}$. Low performance designs do not exhibit NS in the first principal direction. Data from the FE-based homogenization procedure serve as training points for mapping the design and performance spaces, with resulting maps illustrated in Figs. 4.7 and 4.8. The training points were comprised of the 1,000 trials of the Halton sequence, interpolated to span the bounds of each non-dimensional geometric ratio specified in

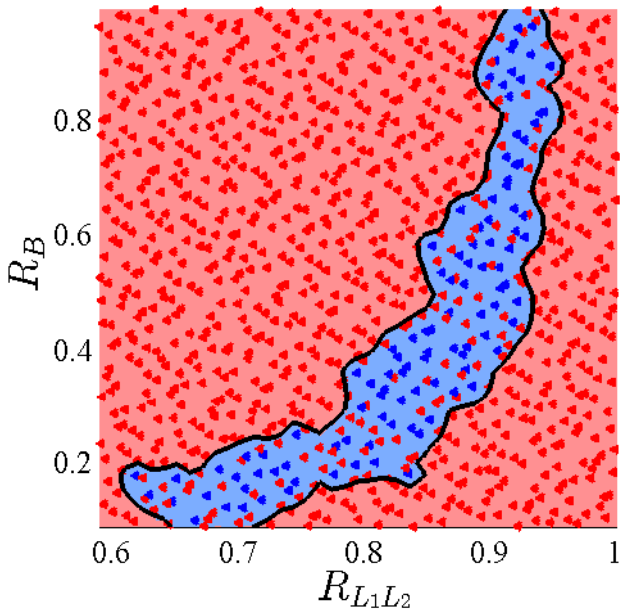

Figure 4.7: Micro → meso scale transition design space mapping: blue points–high performance, red points–low performance.

Table 4.1.

A 2D plot of the microscale design space in Fig. 4.7 maps the high performance design points that exhibit negative values for $C_{11}^{\mathrm{m,eff}}$. High (low) performance points are blue (red), and the black line represents the decision boundary between high and low performance designs. Some of the points within the high performance decision boundary are low performance points, indicated by the red points within the blue region. These points are not incorrectly classified. Rather, they reflect the projection of a 3D design space onto a 2D surface. The R_{L_2T} design variable has only a minor influence on $C_{11}^{\mathrm{m,eff}}$, but changes in its value account for the apparent misclassification of points in Fig. 4.7, which could be eliminated with a 3D plot.

The high performance points in Fig. 4.7 relate to designs in which the four alumina beams shown in Fig. 4.2 buckle due to the induced strains during the thermal contraction of YTZP. The absence of high performance points in the upper left

quadrant of Fig. 4.7 indicates that the induced strain on the beams is insufficient to cause buckling, and supports the notion that a short and thick beam will not buckle. Although not plotted in Fig. 4.7, the design variable R_{L_2T} controls the width of the connector between the alumina beam and the YTZP. This parameter has been bounded to prevent inaccurate point-loading simulation results at the lower bound, and to prevent detrimental effects to the beam buckling characteristics at the upper bound; otherwise, it has little effect on the performance of the inclusion.

All of the design points in Fig. 4.7 map to performance points in Fig. 4.8a, with high performance designs again represented by blue dots. The black lines in Fig. 4.8 represent the boundary of the achievable space, which represents the combinations of performance parameter $C_{11}^{\text{m,eff}}$ and $C_{12}^{\text{m,eff}}$ values that correspond to feasible combinations of design variable ($R_{L_1L_2}$, R_B, and R_{L_2T}) values. The micro $\rightarrow$ meso scale transition model performance space mapping shown in Fig. 4.8a makes it evident that only a small fraction of the design space maps to high performance designs (shown in blue), with attainable $C_{11}^{\text{m,eff}}$ values ranging from 4,000 MPa in positive stiffness to only -80 MPa in NS. Figure 4.8b presents the simulation results and attainable and unattainable performance regions in the strictly high performing ($C_{11} < 0$) case.

4.4 The Meso $\rightarrow$ Macro Scale Transition Model Design Space

In the meso $\rightarrow$ macro scale transition model, the effective stiffness and loss factor are estimated for a composite material, consisting of the NS inclusions dispersed within a viscoelastic matrix. As described in Chapter 3 and Sec. 4.4.1 of the present chapter, effective medium theory (EMT) is used to estimate the effective stiffness and loss properties of the composite. Mappings of the design and performance spaces are described in Sec. 4.4.2.

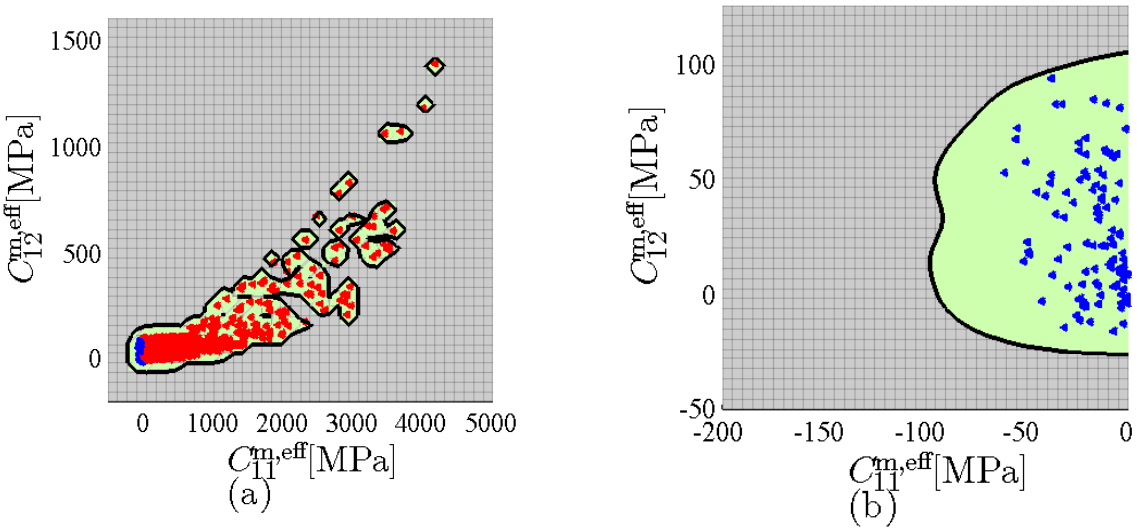

Figure 4.8: (a) Micro → meso scale transition performance space mapping; (b) performance space for high performance case ($C_{11} < 0$). Green shaded areas–attainable design space, gray shaded areas–unattainable design space.

4.4.1 Modeling the Performance of a Composite Material with Negative Stiffness Inclusions

Given the necessary parameters describing the heterogeneous mesoscale, micromechanical EMT is used to predict the macroscale effective stiffness and loss properties of the homogenized composite material. The inputs to the meso → macro scale transition model described in Chapter 3 are the volume fraction, morphology, and orientation of the inclusions within the viscoelastic matrix; the material properties of the matrix; and the effective mesoscale inclusion stiffness tensor. The material properties of the matrix material are assumed to be complex valued (representing a viscoelastic material) and known. The mesoscopic stiffness values of the structured inclusions, on the other hand, have properties determined using the methods described in Sec. 4.3. EMT is a very general modeling approach for estimating quasi-static macroscale stiffness and loss behavior of viscoelastic composite materials [30]. Figure 4.9 depicts the meso → macro scale transition model used in this work, which

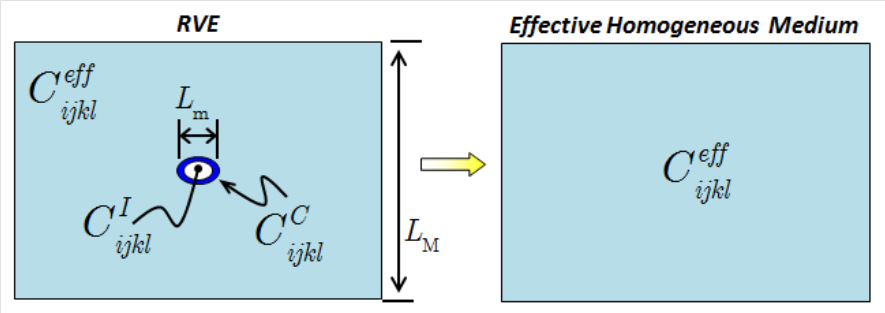

Figure 4.9: Conceptual schematic of the homogenization approach of the Self-Consistent micromechanical model, after Haberman et al. [30].

is a self-consistent model for approximating the effective macroscopic properties of a continuous matrix material containing coated ellipsoidal inclusions. The mesoscale representational volume element (RVE) containing a matrix with stiffness $\mathbf{C}^{\mathrm{M}}$, an inclusion with stiffness $\mathbf{C}^{\mathrm{I}}$, and an inclusion coating with stiffness $\mathbf{C}^{\mathrm{C}}$ is homogenized into a macroscale element with stiffness $\mathbf{C}^{\mathrm{g,eff}}$.

Using these traditionally static models, stiffness and loss behavior of the composite under quasi-static dynamic loading can be modeled via the elastic-viscoelastic correspondence principle. Quasi-static loading conditions are defined as the case where inclusions remain much smaller than the wavelengths induced in the matrix material by dynamic loading and no localized resonances [31]. With these restrictions, the elastic-viscoelastic correspondence principle states that the stiffness tensor of the homogenized composite can be represented with complex valued entities according to Eq. (4.10):

$$\mathbf{C} = \mathbf{C}' + j\mathbf{C}'' = \mathbf{C}'\left(\mathbf{I} + j\boldsymbol{\eta}\right), \tag{4.10}$$

where $\mathbf{C}$ is the complex stiffness tensor consisting of storage, $\mathbf{C}'$, and loss, $\mathbf{C}''$, components, $\mathbf{I}$ is the fourth order identity tensor, and $\boldsymbol{\eta}$ is the loss factor tensor. Under this principle, the usual operations applicable to EMT hold and the overall absorptive

Table 4.2: Meso → macro scale modeling parameters.

Parameter	Variable	Value
Matrix Young's Modulus	Y^{M}	30 MPa
Matrix Poison's Ratio	ν^{M}	0.3
Matrix Loss Factor	η^{M}	0.005
Inclusion Volume Fraction		0.2%

properties of the composite can be estimated [30].

Whereas the inclusions exhibit a highly anisotropic elastic response, an overall isotropic response of the composite is estimated by adding a small volume fraction (0.2%) of inclusions with random orientation, and the effective properties are then found using orientational averaging, as reported in Haberman et al. [30]. The relevant matrix material properties used in this study are given in Table 4.2.

4.4.2 Mapping the Meso → Macro Scale Transition Design Space

The design variables of the meso → macro scale transition model include the $C_{11}^{\mathrm{m,eff}}$ and $C_{12}^{\mathrm{m,eff}}$ elements of the effective mesoscale stiffness tensor, $\mathbf{C}^{\mathrm{m,eff}}$, of the inclusion; the results presented in Chapter 3 indicate that these two elements have the largest performance impact on macroscale performance. The model has two performance variables, namely, the effective stiffness and loss factor of the composite material, defined by the real and imaginary component of the complex valued stiffness tensor of the homogenized composite described in Eq. (4.10).

The mapping of the meso → macro scale model classifies the design and performance spaces into high performance, low performance, and unattainable regions. High performance designs provide a loss factor greater than twice that of the matrix material. The meso → macro scale design space mapping is illustrated in Fig. 4.10. The

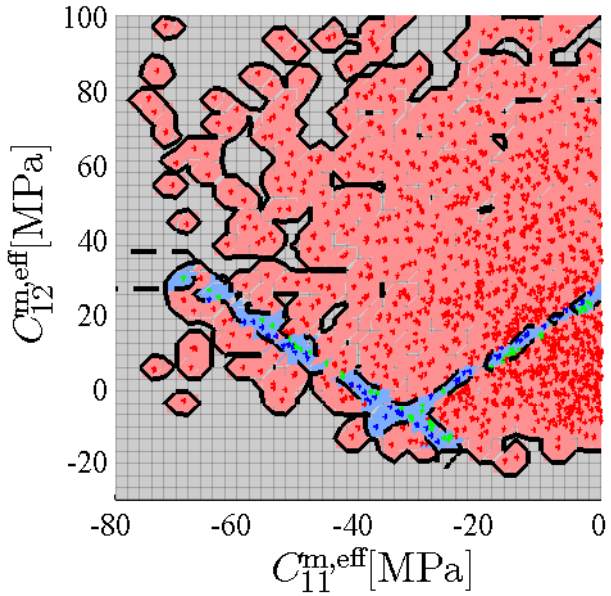

Figure 4.10: Meso → macro scale design space mapping: red–low performance; blue–high performance with macroscale stiffening; green–high performance without stiffening. Gray reflects unattainable design region.

solid black lines indicate the boundary of the achievable space, which is transferred from the micro → meso scale performance map in Fig. 4.8. Within that achievable space, the red dots indicate low performance designs that do not meet the loss factor threshold. The blue and green dots represent designs with high performance, with the blue dots also meeting a minimum threshold for effective stiffness of the homogenized composite (specifically, the effective stiffness of the composite must be greater than or equal to that of the matrix material). The design space mapping illustrates the narrow band of designs that provide high macroscopic performance, wherein only 5% of the meso → macro scale design space was classified as high performance.

Further analysis of the high performance design space of the meso → macro scale model demonstrates intriguing trends. Setting the $C_{11}^{\mathrm{m,eff}}$ stiffness value equal to -20 MPa and unilaterally progressing along the $C_{12}^{\mathrm{m,eff}}$ stiffness value yields the plot shown in Fig. 4.11. The bell-shaped normalized loss curve $\left(\eta^{\mathrm{g,eff}}/\eta^{\mathrm{M}}\right)$ in Fig. 4.11

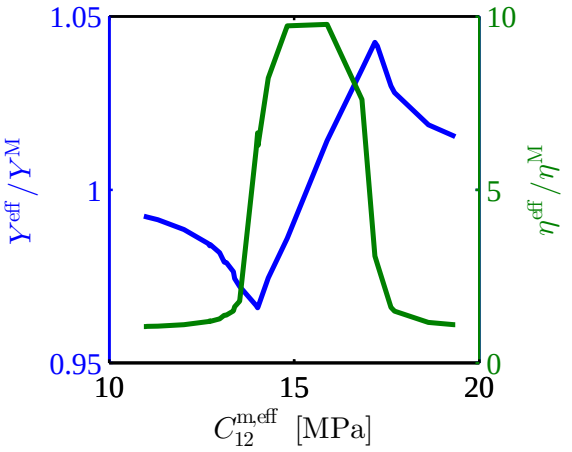

Figure 4.11: The effective stiffness and loss ratio of the composite as a function of $C_{12}^{\mathrm{m,eff}}$, with $C_{11}^{\mathrm{m,eff}} = -20$ MPa.

is to be expected, as the loss factor increases as the design gets closer to its "sweet spot". The stiffness curve $\left(Y^{\mathrm{g,eff}}/Y^{\mathrm{M}}\right)$ in Fig. 4.11 decreases prior to the sweet spot and increases afterwards; a trend that has been shown by Lakes [12] and recent work by the author [68].

The narrow high performance bands shown in Fig. 4.10 indicate a linear relationship between $C_{11}^{\mathrm{m,eff}}$ and $C_{12}^{\mathrm{m,eff}}$ for high performance designs. This trend is explicitly shown in Fig. 4.12. The trend line relates the high performance space to a constant sum of $C_{11}^{\mathrm{m,eff}}$ and $C_{12}^{\mathrm{m,eff}}$. These two constants can be related to the plane-strain bulk modulus, K_{ps}, as illustrated by Eq. (4.11):

$$K_{ps} = \frac{C_{11} + C_{12}}{2}. \tag{4.11}$$

Noting the relationship between $C_{11}^{\mathrm{m,eff}}$ and $C_{12}^{\mathrm{m,eff}}$ and the plane-strain bulk modulus, K_{ps}, given by Eq. (4.11), these results suggest that the high performing designs exhibit a target value for the plain strain bulk modulus which yields desirable overall combinations of stiffness and loss. It is very interesting to note that the results shown in Figs. 4.11 and 4.12, echo results previously published by Lakes [12], which indicate

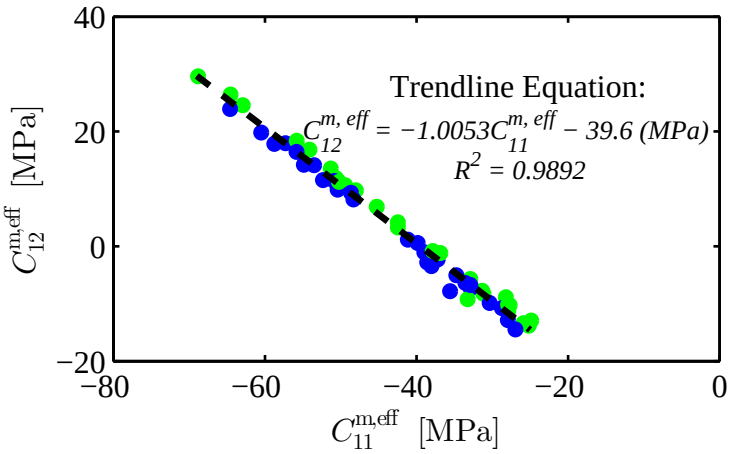

Figure 4.12: A trend line of the meso → macro scale design space for high performance data points: blue–macroscale stiffening; green–decrease in macroscale stiffness.

that specific ratios of inclusion to matrix shear moduli result in drastic increases in the loss factor of the composite.

The y-intercept of the linear trend shown in Fig. 4.12 is specific to the particular matrix stiffness chosen in this experiment. One observes that the intercept essentially determines the plane-strain bulk modulus of the inclusion that will yield significant increases in the overall lossy behavior of the composite. For this particular case, the ratio of the plane-strain bulk modulus of the inclusion to the bulk modulus of the matrix is approximately -0.02. This ratio may be a useful target for enhanced performance in future studies, though the matrix Poisson's ratio and anisotropy of the inclusion likely influence this value. In general, however, these results provide insight into the relationship between the plain strain bulk modulus of inclusions and matrix stiffness.

Having explored the meso → macro design space, the mapping of the performance space is illustrated in Fig. 4.13. The colors of the design points correspond to those in the design space map in Fig. 4.10. The macro-scale performance space clearly demonstrates the benefits of loss and stiffness gained in the high performance

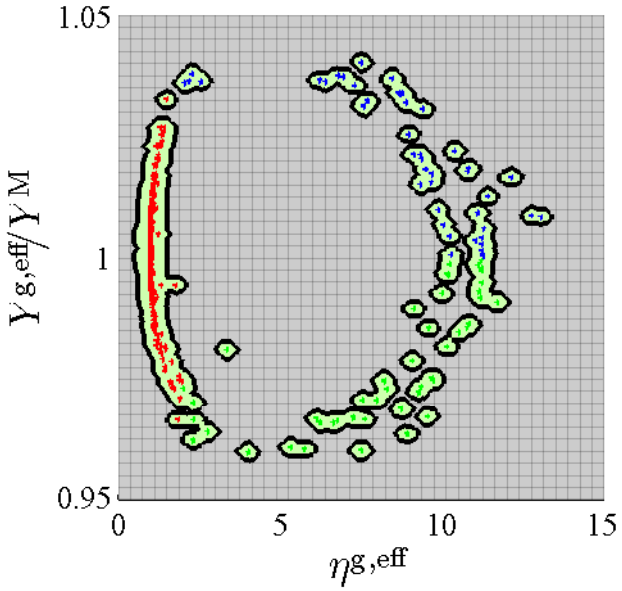

Figure 4.13: Macro-scale performance space mapping: red–low performance; blue–high performance with macroscale stiffening; green–high performance without stiffening. Light green reflects attainable design region; gray–unattainable.

class, as well as the small fraction of points which fall into this class.

The next step is to utilize the micro → meso and meso → macro scale transition model mappings to design a component. This step involves intersecting the smaller-scale performance space mapping with the larger-scale design space mapping to identify multiscale sets of designs that achieve a set of performance requirements for the component. Section 4.5 applies the knowledge of the hierarchical design and performance spaces to the design of a composite coating for passive damping of a structural beam.

4.5 Beam Coating Demonstration Study

In this section, the design and performance space mappings from Sec. 4.4 are used to design a multilayer, cantilever beam coated with a composite material

containing metamaterial inclusions. Section 4.5.1 describes the model for passive viscoelastic damping in a multilayer beam, and Sec. 4.5.2 explores the impact of the design of the composite metamaterial on the shock response of the beam.

Throughout this section, two different coatings are investigated, i) high and ii) low performance, to illustrate the benefit of the approach in Sec. 4.4. The high performance coating corresponds to a design on the border of the blue and green points of Fig. 4.10, while the low performance coating corresponds to a red design point in Fig. 4.13. Specifically, the selected high performance design has an effective coating loss factor, η^{C}, of 0.060, and the low performance design has an effective coating loss factor of 0.005. The high and low performance designs both have equal magnitude effective stiffness, Y^{C}, of 33 MPa. The underlying beam is assumed to be an idealized lossless material with a Young's modulus, Y^{B}, of 1000 MPa.

4.5.1 Loss Factor and Stiffness of a Multilayer, Cantilever Beam

Figure 4.14 illustrates a structural beam coated with a viscoelastic material with microscale inclusions. Ross et al. [69] provide a relationship between the loss factor of the composite beam, η^{eff}, and that of the viscoelastic coating material, η^{C}, according to Eq. (4.12):

$$\frac{\eta^{\mathrm{eff}}}{\eta^{\mathrm{C}}} = \left[1 + \frac{k^2\left(1 + \left(\eta^{\mathrm{C}}\right)^2\right) + \left(r_1/H_{12}\right)^2 a}{k\left(1 + \left(r_2/H_{12}\right)^2 a\right)}\right]^{-1}, \tag{4.12}$$

where H_{12} is the distance between neutral axes of the two layers of a multilayer beam system; the radius of gyration, $r_i = H_i/\sqrt{12}$; $k = K_2/K_1$, where $K_i = Y_i A_i$, where Y_i is the real part of the Young's modulus and A_i is the cross-sectional area of layer i; and a is given by Eq. (4.13):

$$a = (1 + k)^2 + \left(\eta^{\mathrm{C}} k\right)^2. \tag{4.13}$$

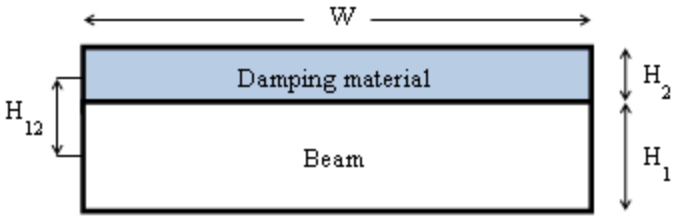

Figure 4.14: Illustration of a beam with a composite coating.

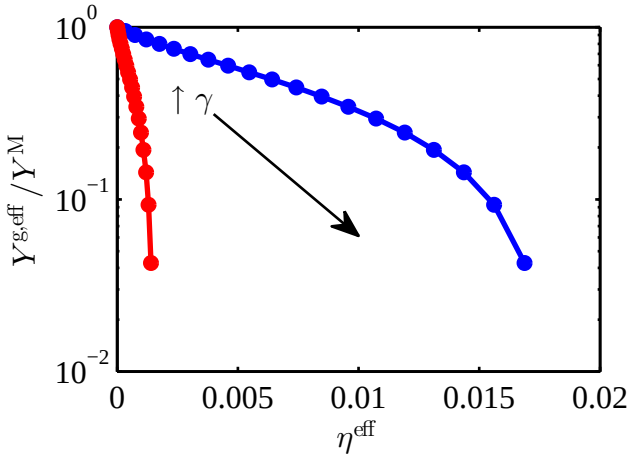

Figure 4.15: Normalized stiffness vs. effective composite loss factor with varying coating thicknesses. Red indicates low performance coating; blue–high performance coating. Arrow indicates direction of increasing γ.

A height fraction of the structural portion of the beam, γ, is given by Eq. (4.14):

$$\gamma = \frac{H_1}{H_1 + H_2}. \tag{4.14}$$

The potential structural benefits of the coating are shown in Fig. 4.15, which displays the normalized effective stiffness of the composite beam versus effective loss factor as a function of the height fraction, γ. The effective stiffness, Y^{eff}, of the composite beam was calculated using the Voigt approximation [70], and is normalized by the beam stiffness, Y^{B}, in order to demonstrate the effect of the coating on the overall stiffness of the composite beam. The effective loss factor of the composite, η^{eff}, was determined from Eq. (4.12).

As shown in Fig. 4.15, the composite beam loss factor increases with increasing coating thickness. For the high performance coating, this increase occurs at a much greater rate relative to the low performance coating, while both high and low performance coatings experience equivalent decreases in the overall stiffness of the beam. This trend is expected because the high and low performance designs were chosen to have equivalent effective stiffnesses but with very different effective loss factors.

The plot shown in Fig. 4.15 could be used to engineer a multilayer system with desired stiffness and loss characteristics based solely on the height fraction. At a height fraction, γ, of 0.2, the effective composite stiffness is decreased by 19%, with a loss factor, η^{eff} of the high performance composite of 0.0017 and a loss factor of the low performance coating of 0.00014. Similarly, if the coating-to-beam height ratio increased to 0.5, the effective composite stiffness of both designs are decreased by 48%, with a resulting loss factor of the high performance composite of 0.0064 and a loss factor of the low performance coating of 0.00053.

4.5.2 Transient Response of the Multilayer Cantilever Beam to an Impulsive Load

To demonstrate the performance enhancements associated with the energy absorbing coating, the coated beam is assembled in a cantilever orientation, as shown in Fig. 4.16, and subjected to an impulsive load at its free end. It is assumed that the length, L, and width, W, of the cantilever beam are 1 m and 0.2 m, respectively. The overall cross-sectional height of the beam, $H_1 + H_2$, is assumed to be 0.1 m, and the individual heights of the beam and viscoelastic material are determined by γ in Eq. (4.14). The density of the beam is assumed to be 1,000 kg/m^2, and the density of the viscoelastic material is assumed to be 200 kg/m^2. Although the cantilever beam is an idealized structural component, it helps illustrate the potential value of the NS

Figure 4.16: An illustration of the coated cantilever beam with an impulsive load imposed at its free end at $t = 0$.

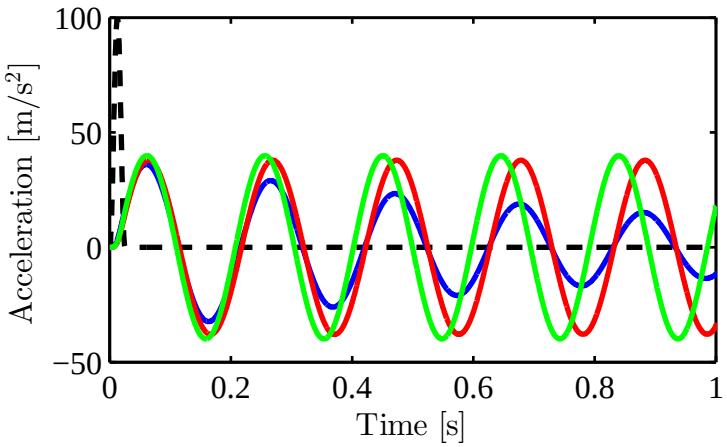

Figure 4.17: The coated and uncoated cantilever beam shock response. Dashed black line indicates shock input; green line–uncoated beam; red–low performance coating; blue–high performance coating.

composite for vibro-acoustic dampening applications.

The height fraction for this demonstration study was chosen based on Fig. 4.15 to exhibit one order of magnitude decrease in stiffness, which corresponds to γ of 0.93. For this choice of coating height, the loss factors for the high and low performance composites are 0.015 and 0.0013, respectively. For this experiment, the beam tip is subjected to a 10 g magnitude versine shock input with a 25 ms duration starting at $t = 0$. The resulting tip displacement for two cases of interest is plotted in Fig. 4.17.

As shown in Fig. 4.17, the tip displacements of the two composite beams exhibit oscillating ringdown, because neither composite is critically damped. The high performance coating causes the beam to ring down significantly faster than the

low performance coating, however, and both are a profound improvement over the underlying beam alone, which would theoretically oscillate forever. The high performance composite is 0.75% critically damped, while the low performance composite is 0.065% critically damped. This is equivalent to a log decrement of -0.047 for the high performance composite and -0.0041 for the poor performance composite. The high performance composite attenuates the acceleration to 0.7% of its initial acceleration amplitude after 10 seconds, while the poor performance coating composite attenuates its acceleration amplitude to only 65% of its initial amplitude during the same time period. The acceleration attenuation of the high performance composite equates to a time constant of 2.04, while the poor performance composite has a time constant of 23.5. To summarize, the high performance coating provides much more efficient damping, exhibiting an order of magnitude improvement in log decrement and an order of magnitude decrease in time constant in comparison with the low performance coating.

4.6 Closure

In summary, this chapter has presented the implementation and results of a multiscale modeling approach, capable of engineering macroscale materials with enhanced energy absorption based on embedded constituents with particular microstructural features. Section 4.3 introduced the idea of geometry-dependent stiffness for microscale inclusions subjected to thermal mismatch buckling. A metamodel of stiffness as a function of geometric parameters was developed and used to map the micro $\rightarrow$ meso scale transition design and performance spaces. These results were incorporated into the meso $\rightarrow$ macro scale transition model results presented in Sec. 4.3. Design and performance maps were created at this scale, and high and low performance materials were selected for use in a composite beam demonstration in

Sec. 4.5. The composite beam demonstration revealed marked improvement of the high performance coating over the low performance coating.

The results presented here suggest that viscoelastic materials containing even very low volume fractions (0.2%) of structured NS inclusions display drastic increases in energy absorption and loss factor as well as providing the capability to tailor the stiffness at the macroscale. Further, because the effective properties of the composite can be tuned by adjusting the properties of the inclusion and the inclusion properties can be tailored through its microscale structure, the modeling approach presented in this work can be leveraged to achieve macroscopic performance exceeding those of currently available materials. It is also interesting to note that the generality of the multiscale model can easily be altered to offer more complex behavior, such as high damping in one direction and low in another, simply by altering the microscale structure. This chapter presents a hierarchical model leading to total inverse design. This approach implements cascading models and techniques to specify microscale inclusion parameters such as geometry, volume fraction, and orientation distribution, based on requirements at the macroscale. Results from the models can be propagated in the reverse direction as well.

Chapter 5

Design, Build, and Test of Prototype Negative Stiffness Inclusions

Whereas the models and results presented in Chapters 3 and 4 have centered around a negative stiffness (NS) inclusion design based on a mismatch of thermal expansion, this chapter explores the fabrication and test of NS elements by means of an alternative manufacturing approach. One objective of this research is to perform experimental testing on a proof-of-concept element. Although micro-coextrusion is a well established manufacturing process, attempts to produce an NS inclusion by this means were unsuccessful and motivated the pursuit of other means of fabrication. Micro-coextrusion is an excellent candidate for dramatically decreasing the element size, but is a rather complicated process for producing relatively simple proof-of-concept measurements. This chapter presents the design of and test results for prototype NS inclusions fabricated by Selective Laser Sintering (SLS). Section 5.1 introduces the idea of a curved beam bistable element, as well as the design, simulation, and fabrication of two prototype elements. Section 5.2 presents the test results of NS elements produced by SLS, and compares the experimental results with analytical and finite element predictions.

5.1 Negative Stiffness via a Curved Beam

In work related to micro-electromechanical systems (MEMS) switches, Qiu et al. [24] present an attractive manner to obtain NS based on microscale geometry.

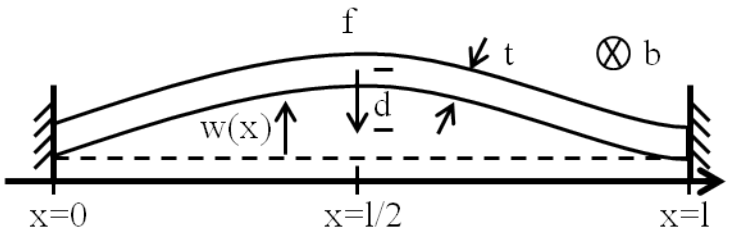

Figure 5.1: Geometry of a curved beam, adapted from Qiu et al. [24].

They establish and verify through experiment that a bistable element which exhibits NS behavior can be generated by fabricating a beam that has a curved shape, as described by Eq. (5.1),

$$\bar{w}\left(x\right) = \frac{h}{2}\left[1 - \cos\left(2\pi\frac{x}{l}\right)\right]. \tag{5.1}$$

In Eq. (5.1), $\bar{w}\left(x\right)$ is the average distance of the beam from the straight line connecting its two endpoints, h is the apex of the beam, x is the lateral position along the straight line connecting the beam's endpoints, and l is the beam span. Figure 5.1 depicts the geometric parameters of interest in the curved beam. The associated force-displacement relation of the curved beam shown in Fig. 5.1 is given by Eq. (5.2):

$$F = \frac{3\pi^4 Q^2}{2}\Delta\left(\Delta - \frac{3}{2} + \sqrt{\frac{1}{4} - \frac{4}{3Q^2}}\right)\left(\Delta - \frac{3}{2} - \sqrt{\frac{1}{4} - \frac{4}{3Q^2}}\right). \tag{5.2}$$

In that expression, the normalized force, F, is given by the relation, $F = fl^3/\left(YIh\right)$, where f is the applied force, Y is the Young's modulus of the beam material, and I is the moment of inertia of the beam. The variable Q is a geometry constant and is given by the relation, $Q = h/t$, where t is the beam thickness. Finally, Δ is the normalized displacement and is given by the relation, $\Delta = d/h$, where d is the displacement in the transverse direction.

Equation (5.2) can be used to design inclusions or structures with desired force-displacement behavior, and thus, the desired stiffness. For example, Fig. 5.2 shows the force-displacement relations of beams with different Q values, given the properties

Table 5.1: Beam design values.

Property	Value
Y (GPa)	1.27
l (in)	1
h (in)	0.1
b (in)	1

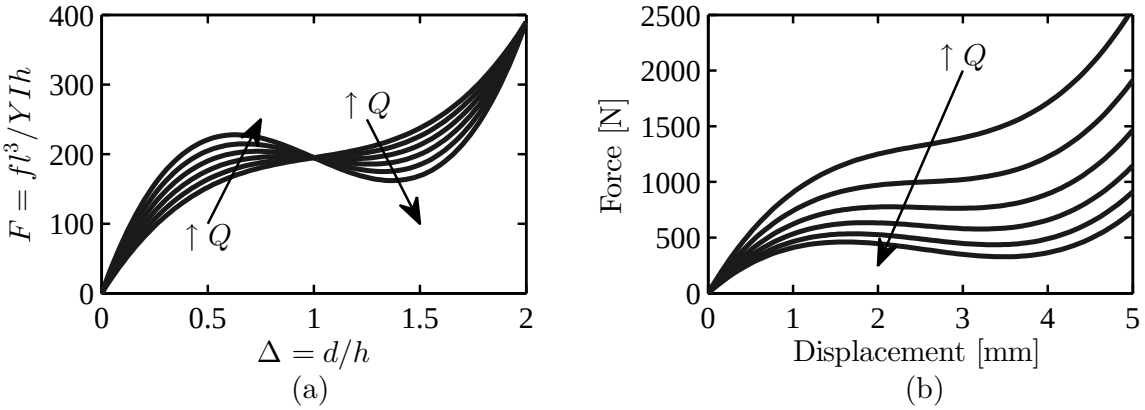

Figure 5.2: Force-displacement relation for a range of Q values from 1 to 1.5 in increments of 0.1: (a) normalized and (b) actual force and displacement values.

contained in Table 5.1. That figure shows both the normalized (panel (a)) and actual (panel (b)) force-displacement responses, and clearly demonstrates the usefulness of Eq. (5.2) as a design tool for obtaining a specific response. For example, a beam with $Q = 1$ yields a monotonically-increasing force-displacement curve (i.e., strictly positive stiffness); when $Q \approx 1.2$, one observes an almost flat force-displacement curve (i.e., quasi-zero stiffness); and when $Q = 1.5$, a negative force-displacement slope (i.e., NS) is observed. Note that while a beam with a $Q = 1.5$ exhibits NS, it is nevertheless monostable because any positive displacement results in a strictly positive force. In other words, for bistability to occur, the force must be less than zero for a particular range of positive displacements. This is is explored further in Sec. 5.1.1.

The stiffness of a curved beam can be calculated as the first partial derivative of the force function with respect to displacement. This is calculated for a range of

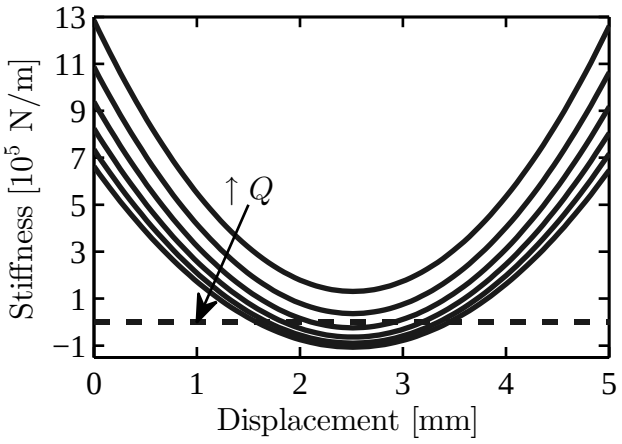

Figure 5.3: Stiffness vs. displacement for a range of Q values from 1 to 1.5 in increments of 0.1.

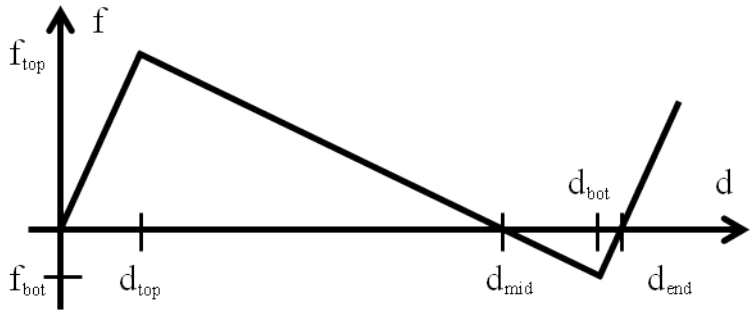

Figure 5.4: Piecewise linear force-displacement curve for a constrained curved beam with $Q \gg 1$ [24].

Q values and shown in Fig. 5.3. The trends discussed in the preceding paragraph are clearly shown, as well as the observation that the nonlinear stiffness values asymptotically approach a certain stiffness value. There is a finite stiffness limit for a beam based on material properties and geometry related to the Q value. As Q increases, the stiffness of the beam reaches a limit, and the force-displacement relationship reflects a piecewise linear function. This is further discussed in Sec. 5.1.1.

5.1.1 Bistability

With regards to manufacturing an element with bistability, Qiu et al. [24] point out that a beam with 2nd-mode buckling constrained (which could be achieved, for example, by coupling it with another curved beam,) will be bistable for $Q > 2.31$. Failure to limit the 2nd-mode deformation will prevent the beam from exhibiting sufficient NS to lead to bistability. Futhermore, Qiu et al. [24] provide approximate values to construct piecewise linear force-displacement relations under the assumption that $Q \gg 1$. This function is represented in Fig. 5.4 and by the equations for force and displacement given by Eqs. (5.3) and (5.4), respectively:

$$f_{top} \approx 740\frac{YIh}{l^3}; \quad f_{bot} \approx -370\frac{YIh}{l^3}; \tag{5.3}$$

$$d_{top} \approx 0.16h; \quad d_{mid} = \frac{4}{3}h; \quad d_{bot} \approx 1.92h; \quad d_{end} \approx 1.99h. \tag{5.4}$$

5.1.2 Design and Simulation of Prototype NS Inclusions

While Eqs. (5.3)–(5.4) give the approximate values to design a beam with bistability, this concept is reserved for future work. The experimental work presented here focuses on producing beams with low Q values as a proof of concept for the generation of NS elements by design. Equation (5.2) was used to generate the parameters for beams with desired stiffness. These beams were then integrated into a larger structure akin to that of the thermal mismatch inclusions, as discussed in Chapter 3. That is, the beam was coupled with a T-shaped interface and integrated into a supporting frame. Figure 5.5 shows the computer-generated solid models of the two different inclusions that were designed with parameters contained in Table 5.2.

Table 5.2: Design parameters for prototype SLS inclusions.

Property	"Large" Element Value	"Small Element" Value
Y (GPa)	1.27	1.27
l (in)	1	0.5
h (in)	0.1	0.05
b (in)	1	0.5
Q	2	1.67

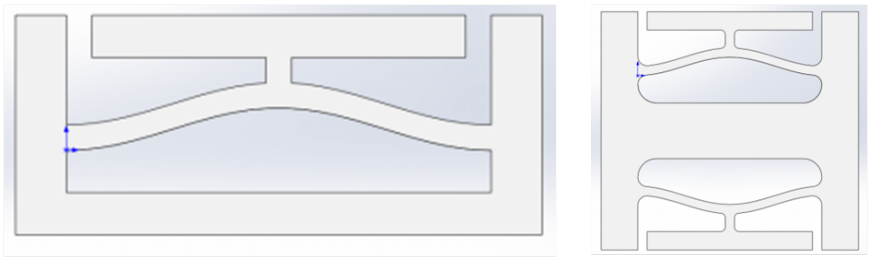

(a) (b)

Figure 5.5: Solid model renderings of NS inclusion prototypes: (a) "large" and (b) "small" elements.

FEA was performed on the prototype inclusion designs in order to validate the curved-beam approach for obtaining NS developed by Qiu et al. [24]. The FEA results are compared with the analytical prediction for both the large and small elements in Figs. 5.6 and 5.7, respectively. The results indicate strong agreement between the FEA and analytical predictions. The resulting force-displacement response is plotted in panel (a) of each figure, and the calculated stiffness-displacement is shown in panel (b). For the large element, both the force- and stiffness-displacement responses are very similar between the analytical prediction and the FEA. One must keep in mind that the FEA considers a beam with elastic boundary conditions, whereas the analytical expression considers beams with fixed ends only. This is believed to be the primary source of discrepancy between the analytical and FEA model results.

Similar trends for the small element force- and stiffness-displacement results are shown in Fig. 5.7. There is very good agreement between the two models. These

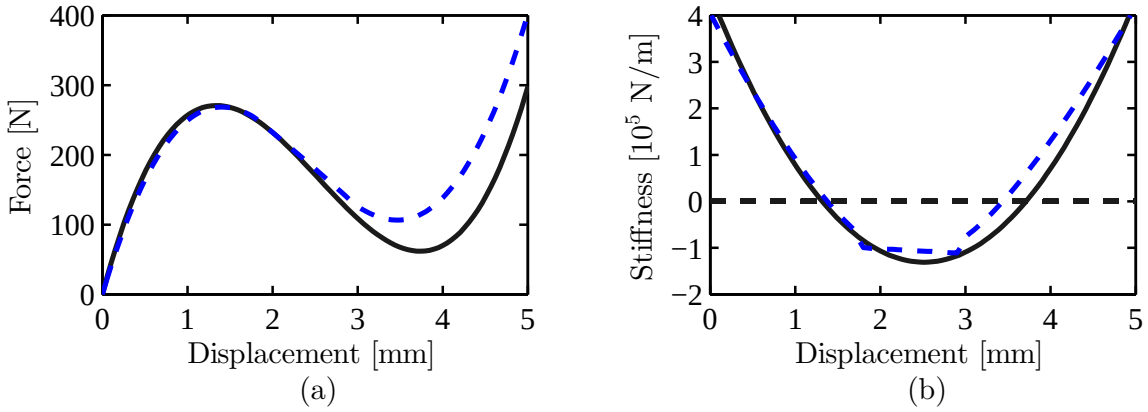

Figure 5.6: Comparison of analytical prediction (black solid line) and FEA (blue dashed line): (a) force-displacement and (b) stiffness-displacement for the large element prototype inclusion.

results validate using the equations developed by Qiu et al. [24] to design beams and structural elements with certain geometric parameters to obtain desired force- and stiffness-displacement behavior. Furthermore, these results yield high confidence that both element designs shown in Fig. 5.5 will exhibit NS.

5.1.3 Prototype Inclusion Fabrication

Given the NS element designs presented in Sec. 5.1.2, it is of interest to investigate the means to fabricate such elements. Kashdan et al. [4] and Fulcher [5] produced vibration and shock isolation systems with NS elements using SLS. SLS is an additive manufacturing process that can produce complex geometries directly from 3D solid models, and is thus an attractive manufacturing process for producing NS elements with curved beams.

The two inclusion designs described by Fig. 5.5 and Table 5.2 were fabricated on an SLS HiQ Sinterstation Machine using Nylon 11 powder. The machine parameters are contained in Table 5.3. The resulting manufactured inclusions are shown in Fig. 5.8.

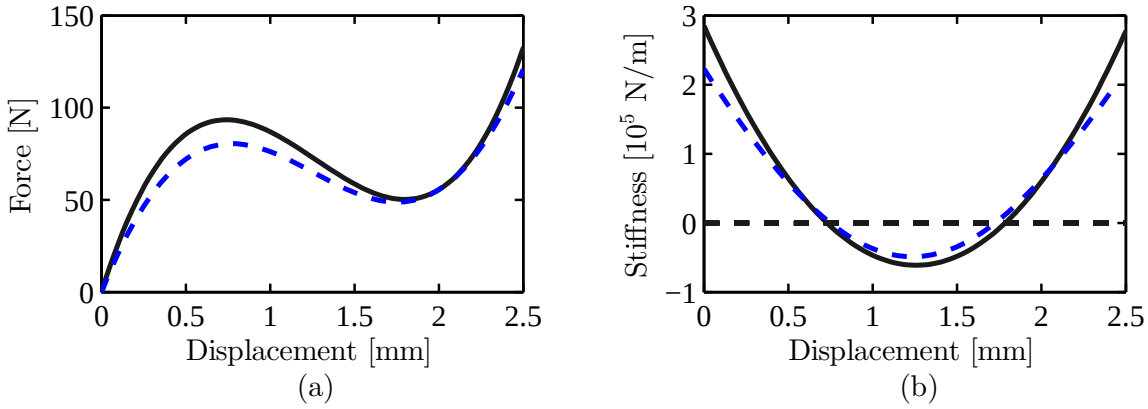

Figure 5.7: Comparison of analytical prediction (black solid line) and FEA (blue dashed line): (a) force-displacement and (b) stiffness-displacement for the small element prototype inclusion.

Table 5.3: Machine parameters for 3D Systems Sinterstation HiQ.

Parameter	Setting
Part Bed Temperature	187 °C
Feed Bin Temperatures	142 °C
Laser Power	38 W
Inner/Outer Ratio	0.8
Scan Spacing	0.01 in
Layer Time	20 s
Layer Thickness	0.0004 in
Roller Speed	10 in/s

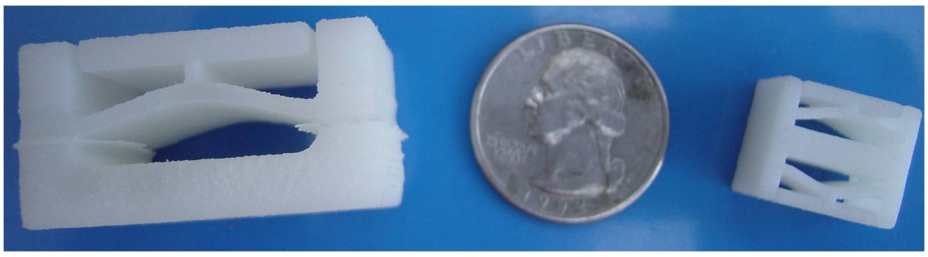

Figure 5.8: Proof-of-concept prototype inclusions manufactured using SLS.

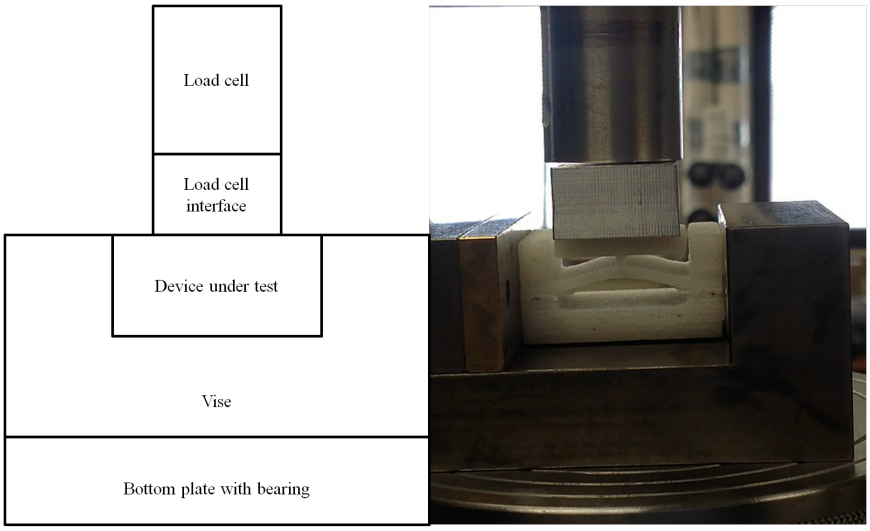

Figure 5.9: Test setup for quasi-static force-displacement testing: (a) schematic with key components labeled and (b) actual test setup photograph.

5.2 Quasi-Static Force-Displacement Testing of NS Inclusion

The prototype inclusions manufactured using SLS were tested to verify the predicted force-displacement relationship. The inclusions were tested using an MTS Sintech 2/G test frame equipped with a 10,000 N load cell. The test setup is shown in Fig. 5.9. A range of displacements was applied to the top of the T-shaped interface and the reaction force as a function of displacement was monitored by the load cell. This particular test stand is equipped with a bearing-mounted bottom platform which allows for self-righting of the platform. An aluminum block was fabricated to sit atop the T-shaped interface of the inclusion to ensure flatness with respect to the load cell. Finally, the NS element was mounted in a steel vise, which provided a zero-displacement boundary condition, when desired, at the edges of the NS element.

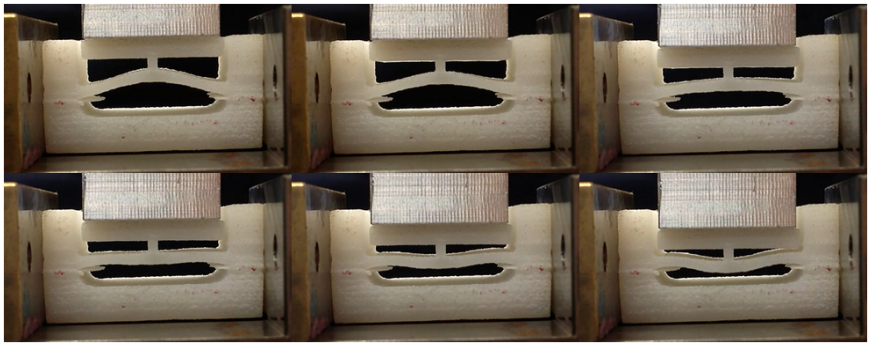

Figure 5.10: Example deformations during force-displacement testing.

5.2.1 Test Results

This section presents the test results for both the large and small NS elements. Each sample was tested multiple times to assess the repeatability of the force-displacement relationship, and to monitor any plastic (permanent) deformation of the elements.

5.2.1.1 Large Element Test Results

Figure 5.10 shows example deformations of the large NS element during testing with a constrained boundary condition applied to the edges. The large and nonlinear displacements of the beam element are evident as the displacement applied at the top of the element is increased. The resulting reaction force is shown in Fig. 5.11a.

The results for the large element with zero-displacement and free boundary conditions are shown in Fig. 5.11a and 5.11b, respectively. The black data points and arrows indicate the loading path (displacement applied downwards), and the blue data points and arrows indicate the unloading path. Figure 5.11a shows that with a constrained boundary condition, the large element exhibits NS over a range of displacements of approximately 1.75 to 3.5 mm. Furthermore, Fig. 5.11a shows that the force-displacement relationship is highly repeatable (at least in the case of

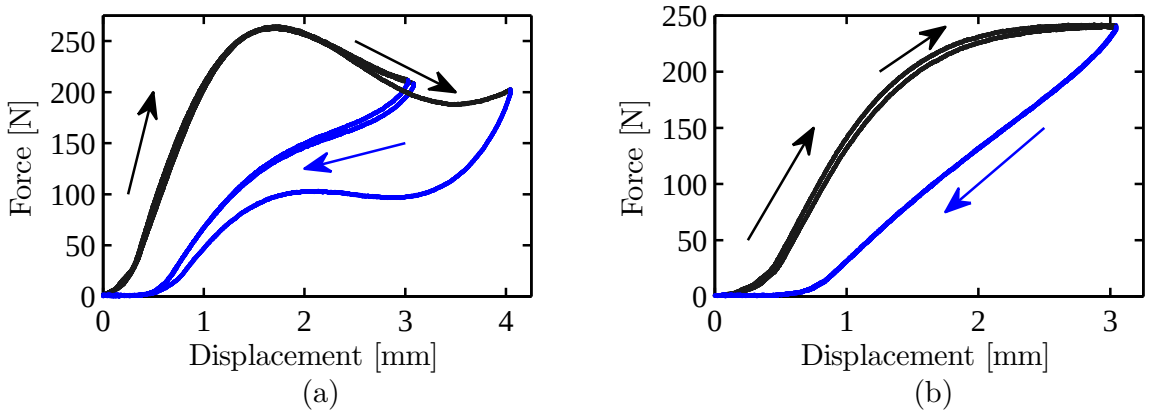

Figure 5.11: Experimental force-displacement curves for large element with (a) zero-displacement and (b) free boundary condition. Black data points and arrows indicate results for the loading, and blue data points and arrows the unloading path.

loading), even for different displacement amounts.

Figure 5.11a shows that the inclusion has a different force-displacement relationship depending on the direction of loading. When the inclusion is unloaded after having been compressed, the results do not follow the loading curve. Furthermore, Fig. 5.11a shows that for different displacements, the force-displacement relation differs on the unloading path. This is most likely due to internal material losses, which have been investigated experimentally in previous work with Nylon 11 SLS components [3]. The objective of this work is to investigate structures that exhibit NS behavior, and not necessarily internal material losses, so this has not been investigated further in this work. Future work could include incorporating the loss factor of Nylon 11 into a viscoelastic FEA model in order to more accurately predict the full-cycle force-displacement curve. Figure 5.11b depicts the effect of easing the constraints on the edges of the inclusion. With the boundary constraint free, the inclusion no longer demonstrates NS. This is a result of the increased flexibility of the inclusion frame at its boundaries leading to the elimination of the NS effect. Similar to Fig. 5.11a, Fig. 5.11b also demonstrates repeatable test results as well as different

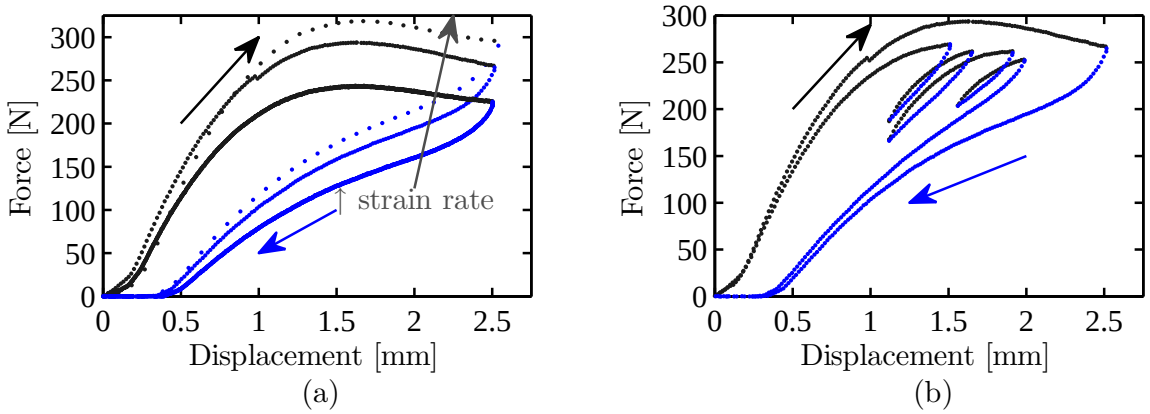

Figure 5.12: Experimental force-displacement curves for large element with zero-displacement boundary condition demonstrating (a) strain rate dependence and (b) minor hysteresis loops. Black data points and arrows indicate results for the loading, and blue data points and arrows the unloading path. In panel (a), direction of increasing strain rate is shown; specific strain rate values were 2.5, 10 and 50 mm/min.

paths for loading and unloading.

The large NS element was used for two additional demonstrations. First, in order to qualitatively demonstrate the viscoelasticity of Nylon 11, the large NS element was tested with three different strain rates. The results are shown in Fig. 5.12a, which indicates a strain rate dependence of the large element force-displacement. This is due to a well-known viscoelastic effect, that for any given temperature, increased strain rate leads to increased stiffness. Furthermore, this effect is also the root cause of the increased force threshold seen in Fig. 5.12a. Future work could consider this information in order to create more accurate material models of Nylon 11. Second, the large NS element was tested by applying several short duration loading and unloading events after the onset of NS in order to demonstrate minor hysteresis loops in the force-displacement relationship. The results are shown in Fig. 5.12b. A baseline force-displacement experiment result is included for reference. The results indicate that the slope of the force-displacement response is similar to the baseline even when there is a series of loading and unloading steps within one all-encompassing test run.

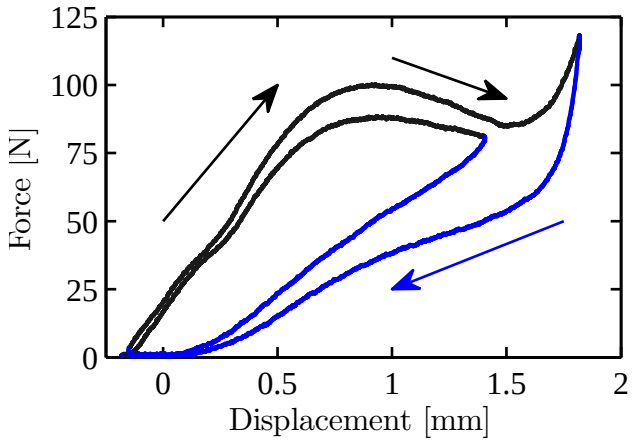

Figure 5.13: Experimental force-displacement curves for small element with zero-displacement boundary condition. Black data points and arrows indicate results for the loading, and blue data points and arrows the unloading path.

The results indicate the even when the loading is cycled in minor hysteresis loops, the NS element continues to demonstrate NS behavior consistent with baseline results. These results yield insight into using structures like the NS element in vibro-acoustic applications, where perturbations would be relatively very small about a given strain state.

5.2.1.2 Small Element Test Results

Figure 5.13 shows the force-displacement curve of the small NS element with constrained edges. The results are repeatable and demonstrate NS (albeit smaller in magnitude compared with the large element, as predicted) over a range of displacements of approximately 1 to 1.6 mm. The sharp peak after the NS on the curve for displacements greater than 1.7 mm is due to the limited travel of the beam element. Beyond approximately 1.7 mm compression, the beam element contacted the supporting frame which yields dramatically increased stiffness.

5.2.2 Comparison of FEA Predictions and Test Results

Having repeatable test results for two different geometries and two different boundary conditions allowed for benchmarking the FEA model. As noted by Fulcher [5], SLS is a relatively imprecise manufacturing technique due to issues such as over-sintering. In this work, taking a few spot-check measurements of the as-built dimensions of the prototype inclusions revealed differences from the as-designed dimensions. For example, whereas the curved beam was designed with a constant thickness, t, the as-built elements demonstrated a non-constant thickness, whose effects on force-displacement behavior are difficult to quantify. The effects of these geometric differences are revealed in Figs. 5.14 and 5.15 for both the large and small NS elements, as the force-displacement curves do not exactly match. A comparison of the quasi-static test results and the FEA predictions of the large element response for constrained and free boundary conditions is shown in panels (a) and (b), respectively, of Fig. 5.14. It is worth noting that only the loading path is compared with the FEA results, as the FEA model did not incorporate material losses to model the full-cycle response. Although, not an exact match, the FEA results reflect distinct similarities with the test data. First, NS behavior is observed, and occurs over a similar range of displacements at a similar force threshold. Also, obtaining similar results for two different boundary conditions further benchmarks the FEA model against the test data.

A similar comparison is made for the small element response with a constrained boundary condition only, and is shown in Fig. 5.15. The results reflect differences between the FEA and test data similar to the large NS element, but indicate that indeed the FEA models of the two different inclusions were able to predict relatively accurately the force-displacement response of both inclusions and boundary condi-

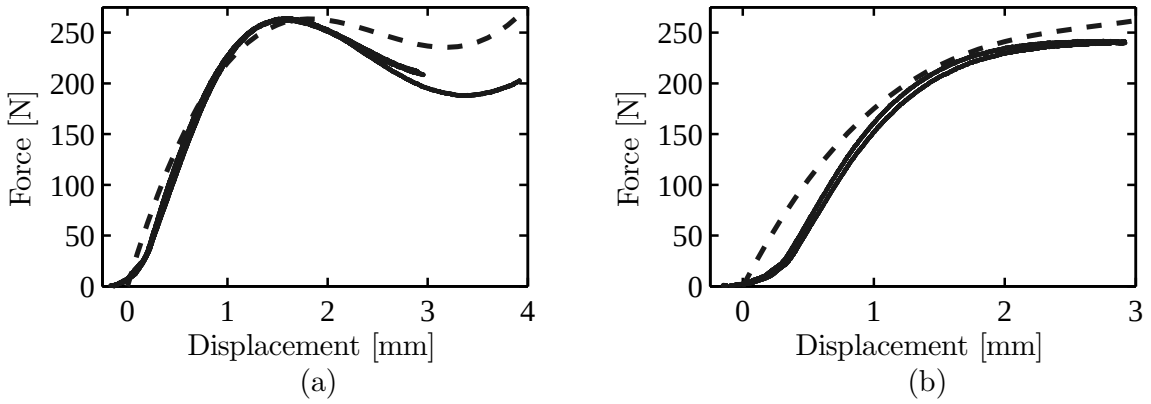

Figure 5.14: Comparison of large element experimental (loading path only) and FEA force-displacement curves: (a) zero-displacement and (b) free boundary condition. FEA results are plotted with dashed black lines and actual test data are plotted with black data points.

tions.

The results presented in this section demonstrate that it is possible to design and simulate structures exhibiting NS based solely on their geometry. However, while the FEA predictions reflect generally good agreement with the experimental results, the imprecision of SLS fabrication makes it difficult to design to specific stiffness values of the NS structure. A more precise manufacturing process, such as computer numerical control (CNC) machining or other freeform manufacturing, could create structures like the ones explored in this work tuned to exhibit exact stiffness values when higher precision behavior is required.

5.3 Summary

In summary, two prototype NS inclusions were designed, simulated, fabricated by SLS, and tested under quasi-static conditions. NS behavior consistent with analytical and FEA predictions was observed. Repeatable results were obtained and used to benchmark FEA models of the elements. The prototype inclusions exhibited internal

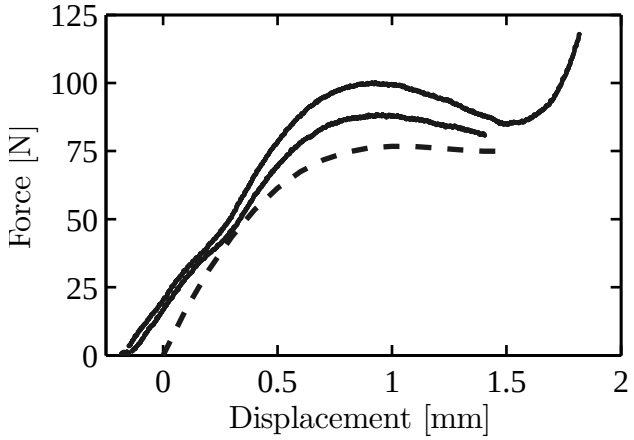

Figure 5.15: Comparison of small element experimental (loading path only) and FEA force-displacement curves with fixed boundary condition. FEA results are plotted with dashed black lines and actual test data are plotted with black data points.

material losses and strain rate dependence, and this test data could be incorporated into more sophisticated viscoelastic material models.

The work presented here validates not only the approach of obtaining NS through geometry, but also SLS as a manufacturing process for producing NS inclusions. Future work could implement the closed-form beam equations into optimization schemes to tailor inclusions. Furthermore, similar manufacturing processes could be investigated to produce similar free-form elements out of alternate materials. Recent developments in stereolithography (SLA) and electrodeposition open the door to manufacturing elements like these out of metals that are much stiffer and possess considerably lower internal material losses. Finally, beam elements with higher Q values could be explored to produce structures with bistability. These elements could be used as either microscale embedded vibro-acoustic energy absorbers, or as macroscale vibration or shock isolation structural components. Whereas other designs rely on either thermal mismatch or mechanical axial compression to induce bistability, these elements have the distinct advantage of possessing NS simply by their geometry.

Chapter 6

Closure

6.1 Summary

The work presented in this thesis has focused on developing energy absorbing composite materials containing negative stiffness (NS) microscale inclusions. While the concept of obtaining extreme damping from these inclusions is well-established in the scientific literature, few, if any, manufacturable inclusion designs exist. This thesis has explored two different manufacturing techniques (micro co-extrusion and Selective Laser Sintering (SLS)) as candidate processes for fabricating energy absorbing NS inclusions. Additionally, two different means of obtaining NS (thermal expansion and curved-beam geometry) have been investigated. One objective at the start of this research was to produce an energy absorbing metamaterial with NS inclusions. While this objective was not fully accomplished, this work nonetheless marks a significant step forward in the design of these highly specialized and engineered materials.

Chapter 3 documents the development of a multiscale material model, starting at the microscale inclusion geometry and ending with the macroscale stiffness and loss properties of a composte material containing these inclusions. A candidate NS metamaterial inclusion is presented in Sec. 3.2, capable of being manufactured by a well-established process. In order to to obtain the nonlinear stiffness properties of the structured inclusion in a manner robust to the effects of the manufacturing process, an energy-based finite element (FE) approach is developed, benchmarked, and employed in Sec. 3.4. Section 3.5 presents the results of the effective medium

theory (EMT) model used in this work to obtain estimates of the macroscale stiffness and loss of a composite material, given matrix properties and inclusion stiffness, volume fraction, and orientation. These results indicate that the composite material indeed demonstrates extreme damping and a tunable stiffness, based solely on the matrix material properties for any particular NS inclusion.

The hierarchical design problem of designing a composite material with NS inclusions is presented in Chapter 4. The NS inclusion geometric framework from Chapter 3 is parameterized in order to obtain geometry-dependent inclusion stiffnesses over a wide range of geometries. Section 4.3 documents the development of a surrogate model that fits a function to the training data obtained from computationally-expensive FE models. Thus, the geometry-dependent stiffness model is further generalized. Given a range of values, the design and performance spaces at the micro $\rightarrow$ meso scale transition are visualized in Sec. 3.4. The performance space from this level is used as the input to the design space at the next, the meso $\rightarrow$ macro scale transition. The design and performance maps at this level are presented in Sec. 4.4. These maps demonstrate very narrow bands of high performance designs, and illustrate the usefulness in obtaining such mappings. Finally, in order to demonstrate the utility of this approach, a multilayer beam system possessing a coating of energy absorbing material is presented in Sec. 4.5. The results from this demonstration indicate the highly absorptive effect of an optimized beam coating consisting of NS inclusions on the beam ringdown and shock response.

Finally, an alternative method for fabricating NS inclusions using additive manufacturing is explored in Chapter 5. The concept of obtaining NS via a curved beam is introduced in Sec. 5.1. Prototype inclusion designs using closed-form expressions for a curved beam are developed, modeled, and ultimately manufactured

using SLS. These elements are tested to verify NS behavior, and compared with the analytical predictions in Sec. 5.2. This chapter validates the approach of obtaining NS via a curved beam geometry, and presents a manufacturable inclusion design.

6.2 Future Work

The work presented in this thesis has advanced research of NS elements through the development and integration of computational material models, as well as the design, fabrication, and test of prototype NS inclusions. Future work could build on each of these areas of research. What follows are some suggested follow-on research activities.

The prototype NS inclusion test data revealed a viscoelastic response of the Nylon 11 material. The models created in this work do not incorporate internal material losses, so the test data matches the predicted force-displacement relationship for the loading case only. If SLS will be used to create embeddable inclusions, or if the inclusions are made of any material with significant viscoelastic losses, then developing a material model complete with internal losses would be prudent and allow for the prediction of the complete loading and unloading force-displacement response.

One key area of concern for virtually any manufacturing process is internal material defects. These defects can be present for any number of reasons. It is easy to imagine manufacturing defects having an effect on the response of an NS element. While this present work has performed no manufacturing defect analysis, models could be created using the same basic approach outlined here, with the addition of creating randomized defects within the inclusion. Performing this analysis could yield insights into manufacturing tolerances and smart ways to create NS inclusions robust to manufacturing defects.

The hierarchical design approach presented in this research reflects a relatively basic demonstration of set-based design. The framework has been established for a multiscale material model starting at the microscale and proceeding through the macroscale to the level of demonstration. An engineer could use this framework to specify desired loss characteristics and intersect that space with the attainable microscale design space. This process could be enhanced using Bayesian classifier networks to further interrogate the design space, develop new capabilities, and gain new insights.

The range of geometries used in this work to train a metamodel led to a vast range of inclusion stiffness. Specifically, the values ranged from approximately -100 MPa to 10 GPa. While the metamodel was able to predict the inclusion stiffness with good accuracy, as reflected in the error metrics, this could be improved. Since the area of particular interest is a relatively low magnitude value of negative stiffness, a two-stage metamodel could be developed. The initial global metamodel could be used to predict stiffness over the entire range from MPa to GPa. Then, if a particular design falls within certain bounds, a second local metamodel could be used to predict the low magnitude stiffness values with higher precision. This would greatly increase the accuracy of predictions in the region of interest.

This work explored the idea of creating NS elements with curved beams by means of SLS. The beams studied in this work were of low apex to thickness values, and thus exhibited NS with monostability. Beams with higher ratios have been shown to exhibit NS and bistability, meaning the beams possess two stable positions. SLS or other freeform manufacturing techniques could be used to produce these NS elements. These elements have the distinct advantage that they do not require pre-compression or thermal mismatch to exhibit NS. Thus, these elements could

be created and utilized as either embedded inclusions if smallscale, or assembled in a larger system if macroscale. A microscale inclusion could be tested acoustically to obtain the composite material effective properties, demonstrating broadband energy absorption. Additionally, on the macroscale, these elements could be used to develop shock and vibration isolation systems, as well as energy harvesting systems (such as by being coupled with piezoelectric components).

Bibliography

[1] M. Brodt and R. Lakes, "Composite materials which exhibit high stiffness and high viscoelastic damping," *Journal of Composite Materials*, vol. 29, no. 14, pp. 1823–1833, 1995.

[2] R. Lakes, T. Lee, A. Bersie, and Y. Wang, "Extreme damping in composite materials with negative-stiffness inclusions," *Nature*, vol. 410, no. 6828, pp. 565–567, 2001.

[3] L. B. Kashdan, "Evaluation of negative stiffness elements for enhanced material damping capacity," Master's thesis, The University of Texas at Austin, 2010.

[4] L. Kashdan, C. C. Seepersad, M. Haberman, and P. S. Wilson, "Design, fabrication, and evaluation of negative stiffness elements using SLS," *Rapid Prototyping Journal*, vol. 18, no. 3, pp. 194–200, 2012.

[5] B. A. Fulcher, "Evaluation of systems containing negative stiffness elements for vibration and shock isolation," Master's thesis, The University of Texas at Austin, 2012.

[6] J. Prasad and A. Diaz, "Viscoelastic material design with negative stiffness components using topology optimization," *Structural and Multidisciplinary Optimization*, vol. 38, no. 6, pp. 583–597, 2009.

[7] J. N. Grima and R. Caruana-Gauci, "Mechanical metamaterials: Materials that push back," *Nature Materials*, vol. 11, no. 7, pp. 565–566, 2012.

[8] J. Jarzynski, "Mechanisms of sound attenuation in materials," *Sound and Vibration Damping with Polymers*, pp. 167–207, 1990.

[9] Z. Hashin, "Complex moduli of viscoelastic composites - I. General theory and application to particulate composites," *International Journal of Solids and Structures*, vol. 6, no. 5, pp. 539–552, 1970.

[10] L. Gibiansky and R. Lakes, "Bounds on the complex bulk modulus of a two-phase viscoelastic composite with arbitrary volume fractions of the components," *Mechanics of Materials*, vol. 16, no. 3, pp. 317–331, 1993.

[11] L. Gibiansky and R. Lakes, "Bounds on the complex bulk and shear moduli of a two-dimensional two-phase viscoelastic composite," *Mechanics of Materials*, vol. 25, no. 2, pp. 79–95, 1997.

[12] R. Lakes, "Extreme damping in composite materials with a negative stiffness phase," *Physical Review Letters*, vol. 86, no. 13, pp. 2897–2900, 2001.

[13] R. Lakes, "Extreme damping in compliant composites with a negative-stiffness phase," *Philosophical Magazine Letters*, vol. 81, no. 2, pp. 95–100, 2001.

[14] Z. G. Nicolaou and A. E. Motter, "Mechanical metamaterials with negative compressibility transitions," *Nature Materials*, vol. 11, no. 7, pp. 608–613, 2012.

[15] N. Fang, D. Xi, J. Xu, M. Ambati, W. Srituravanich, C. Sun, and X. Zhang, "Ultrasonic metamaterials with negative modulus," *Nature materials*, vol. 5, no. 6, pp. 452–456, 2006.

[16] L. Fok, M. Ambati, and X. Zhang, "Acoustic metamaterials," *MRS bulletin*, vol. 33, no. 10, pp. 931–934, 2008.

[17] A. L. Cauchy, "Mémoire sur la polarisation des rayons réfléchis ou refractes par la surface de separation de deux corps isophanes et transparents," *Comptes Rendus*, vol. 9, pp. 676–691, 1839.

[18] W. Thomson, "XLVI. On the reflexion and refraction of light," *Philosophical Magazine Series 5*, vol. 26, no. 162, pp. 414–425, 1888.

[19] E. T. Whittaker, *A History of the Theories of Aether and Electricity*. T. Nelson, 1953.

[20] H. Yap, R. Lakes, and R. Carpick, "Negative stiffness and enhanced damping of individual multiwalled carbon nanotubes," *Physical Review B*, vol. 77, no. 4, p. 045423, 2008.

[21] Y. Wang and R. Lakes, "Extreme stiffness systems due to negative stiffness elements," *American Journal of Physics*, vol. 72, p. 40, 2004.

[22] D. Platus, "Negative-stiffness-mechanism vibration isolation systems," in *SPIE's International Symposium on Optical Science, Engineering, and Instrumentation*, pp. 98–105, International Society for Optics and Photonics, 1999.

[23] T. Mizuno, T. Toumiya, and M. Takasaki, "Vibration isolation system using negative stiffness," *JSME International Journal Series C*, vol. 46, no. 3, pp. 807–812, 2003.

[24] J. Qiu, J. Lang, and A. Slocum, "A curved-beam bistable mechanism," *Microelectromechanical Systems, Journal of*, vol. 13, no. 2, pp. 137–146, 2004.

[25] M. Saif, "On a tunable bistable MEMS-theory and experiment," *Microelectromechanical Systems, Journal of*, vol. 9, no. 2, pp. 157–170, 2000.

[26] R. Lakes and W. Drugan, "Dramatically stiffer elastic composite materials due to a negative stiffness phase?," *Journal of the Mechanics and Physics of Solids*, vol. 50, no. 5, pp. 979–1009, 2002.

[27] M. R. Haberman, *Design of high loss viscoelastic composites through micromechanical modeling and decision based materials design*. Dissertation, Georgia Institute of Technology, 2007.

[28] Y. Fung and P. Tong, *Classical and Computational Solid Mechanics*, vol. 1. World Scientific Publishing Company Incorporated, 2001.

[29] Y. Koutsawa, M. Haberman, E. Daya, and M. Cherkaoui, "Multiscale design of a rectangular sandwich plate with viscoelastic core and supported at extents by viscoelastic materials," *International Journal of Mechanics and Materials in Design*, vol. 5, no. 1, pp. 29–44, 2009.

[30] M. Haberman, Y. Berthelot, and M. Cherkaoui, "Micromechanical modeling of particulate composites for damping of acoustic waves," *Journal of Engineering Materials and Technology*, vol. 128, no. 3, pp. 320–329, 2006.

[31] G. Milton, *The Theory of Composites*, vol. 6. Cambridge University Press, 2002.

[32] M. Haberman, Y. Berthelot, and M. Cherkaoui, "Transmission loss of viscoelastic materials containing oriented ellipsoidal coated microinclusions," *The Journal of the Acoustical Society of America*, vol. 118, p. 2984, 2005.

[33] M. Cherkaoui, H. Sabar, and M. Berveiller, "Micromechanical approach of the coated inclusion problem and applications to composite materials," *Journal of Engineering Materials and Technology*, vol. 116, no. 3, pp. 274–278, 1994.

[34] Z. Yang, J. Mei, M. Yang, N. Chan, and P. Sheng, "Membrane-type acoustic metamaterial with negative dynamic mass," *Physical Review Letters*, vol. 101, no. 20, p. 204301, 2008.

[35] S. Guenneau, A. Movchan, G. Pétursson, and S. Ramakrishna, "Acoustic metamaterials for sound focusing and confinement," *New Journal of Physics*, vol. 9, no. 11, p. 399, 2007.

[36] H. Chen and C. Chan, "Acoustic cloaking in three dimensions using acoustic metamaterials," *Applied Physics Letters*, vol. 91, no. 18, pp. 183518–183518, 2007.

[37] G. E. Box and K. Wilson, "On the experimental attainment of optimum conditions," *Journal of the Royal Statistical Society. Series B (Methodological)*, vol. 13, no. 1, pp. 1–45, 1951.

[38] J. Sacks, S. B. Schiller, and W. J. Welch, "Designs for computer experiments," *Technometrics*, vol. 31, no. 1, pp. 41–47, 1989.

[39] T. W. Simpson, J. Poplinski, P. N. Koch, and J. K. Allen, "Metamodels for computer-based engineering design: survey and recommendations," *Engineering with computers*, vol. 17, no. 2, pp. 129–150, 2001.

[40] J. Sobieszczanski-Sobieski and R. T. Haftka, "Multidisciplinary aerospace design optimization: survey of recent developments," *Structural optimization*, vol. 14, no. 1, pp. 1–23, 1997.

[41] J. Sobieszczanski-Sobieski, J. S. Agte, and R. R. Sandusky, "Bilevel integrated system synthesis," *AIAA journal*, vol. 38, no. 1, pp. 164–172, 2000.

[42] P. B. Backlund, D. W. Shahan, and C. C. Seepersad, "A comparative study of the scalability of alternative metamodelling techniques," *Engineering Optimization*, vol. 44, no. 7, pp. 767–786, 2012.

[43] B.-S. Kim, Y.-B. Lee, and D.-H. Choi, "Comparison study on the accuracy of metamodeling technique for non-convex functions," *Journal of Mechanical Science and Technology*, vol. 23, pp. 1175–1181, 2009.

[44] T. Fujimoto and K. Clark, "Product development performance," *Strategy, Organisation and Management in the World Auto Industry*, 1991.

[45] D. K. Sobek, A. C. Ward, and J. K. Liker, "Toyota's principles of set-based concurrent engineering," *Sloan management review*, vol. 40, no. 2, pp. 67–84, 1999.

[46] A. Ward, I. Durward Sobek, J. C. John, and K. L. Jeffrey, "Toyota, concurrent engineering, and set-based design," *Ch*, vol. 8, pp. 192–216, 1995.

[47] D. Shahan and C. Seepersad, "Bayesian network classifiers for set-based collaborative design," *Journal of Mechanical Design*, vol. 134, no. 7, 2012.

[48] G. Hilmas and G. Brady, "SiC and Si_3N_4 fibrous monoliths: Non-brittle fracture from powder processed ceramics produced by coextrusion," *Ceram. Trans.*, vol. 51, pp. 609–614, 1994.

[49] D. Kovar, B. King, R. Trice, and J. Halloran, "Fibrous monolithic ceramics," *Journal of the American Ceramic Society*, vol. 80, no. 10, pp. 2471–2487, 1997.

[50] C. Hoy, A. Barda, M. Griffith, and J. Halloran, "Microfabrication of ceramics by co-extrusion," *Journal of the American Ceramic Society*, vol. 81, no. 1, pp. 152–158, 1998.

[51] A. Crumm and J. Halloran, "Fabrication of microconfigured multicomponent ceramics," *Journal of the American Ceramic Society*, vol. 81, no. 4, pp. 1053–1057, 1998.

[52] Y. Koh, H. Kim, H. Kim, and J. Halloran, "Fabrication of macrochannelled-hydroxyapatite bioceramic by a coextrusion process," *Journal of the American Ceramic Society*, vol. 85, no. 10, pp. 2578–2580, 2002.

[53] R. M. Christensen, *Mechanics of Composite Materials*. Dover Publications, Inc., 2005.

[54] M. Cherkaoui, Q. Sun, and G. Song, "Micromechanics modeling of composite with ductile matrix and shape memory alloy reinforcement," *International Journal of Solids and Structures*, vol. 37, no. 11, pp. 1577–1594, 2000.

[55] W. Parnell, "Elastic wave scattering from a strained region," Master's thesis, 2000.

[56] W. J. Parnell, "Nonlinear pre-stress for cloaking from antiplane elastic waves," *Proceedings of the Royal Society A: Mathematical, Physical and Engineering Science*, vol. 468, no. 2138, pp. 563–580, 2012.

[57] A. Norris, "Small-on-large theory with applications to granular materials and fluid/solid systems," in *Waves in Nonlinear Pre-Stressed Materials*, pp. 27–62, Springer, 2007.

[58] J. Rose, *Ultrasonic Waves in Solid Media*. Cambridge university press, 2004.

[59] J. Tichỳ, J. Erhart, E. Kittinger, and J. Přívratská, "Basic thermodynamics of piezoelectric crystals," in *Fundamentals of Piezoelectric Sensorics*, pp. 55–68, Springer, 2010.

[60] G. Odegard, "Constitutive modeling of piezoelectric polymer composites," *Acta Materialia*, vol. 52, no. 18, pp. 5315–5330, 2004.

[61] M. Cherkaoui, H. Sabar, and M. Berveiller, "Elastic composites with coated reinforcements: a micromechanical approach for nonhomothetic topology," *International journal of engineering science*, vol. 33, no. 6, pp. 829–843, 1995.

[62] J. D. Eshelby, "The determination of the elastic field of an ellipsoidal inclusion, and related problems," *Proceedings of the Royal Society A: Mathematical, Physical and Engineering Science*, vol. 241, no. 1226, pp. 376–396, 1957.

[63] M. Berveiller, O. Fassi-Fehri, and A. Hihi, "The problem of two plastic and heterogeneous inclusions in an anisotropic medium," *International Journal of Engineering Science*, vol. 25, no. 6, pp. 691–709, 1987.

[64] R. M. Christensen, "A critical evaluation for a class of micro-mechanics models," *Journal of the Mechanics and Physics of Solids*, vol. 38, no. 3, pp. 379–404, 1990.

[65] G. Freeman and J. Halton, "Note on an exact treatment of contingency, goodness of fit and other problems of significance," *Biometrika*, vol. 38, no. 1/2, pp. 141–149, 1951.

[66] P. Backlund, D. Shahan, and C. Seepersad, "Metamodeling techniques for multidimensional ship design problems," *Ship Science & Technology*, vol. 4, no. 7, 2010.

[67] G. R. Ely and C. C. Seepersad, "A comparative study of metamodeling techniques for predictive process control of welding applications," *ASME Conference Proceedings*, vol. 2009, no. 43611, pp. 395–407, 2009.

[68] T. Klatt and M. R. Haberman, "A nonlinear negative stiffness metamaterial unit cell and small-on-large multiscale material model," *Journal of Applied Physics*, vol. 114, no. 3, p. 033503, 2013.

[69] D. Ross, E. E. Ungar, and E. Kerwin, "Damping of plate flexural vibrations by means of viscoelastic laminae," *Structural damping*, vol. 3, pp. 44–87, 1959.

[70] W. Voigt, "Ueber die beziehung zwischen den beiden elasticitätsconstanten isotroper körper," *Annalen der Physik*, vol. 274, no. 12, pp. 573–587, 1889.